Development of Time Projection Chamber for Experiments with Heavy Ion Collisions

Tadaaki Isobe

Master's Thesis

Department of Physics
Graduate School of Science
University of Tokyo
7-3-1 Hongo, Bunkyo-ku, Tokyo 113-0033, JAPAN

2 February, 2004

Contents

List of Figures

List of Tables

Chapter 1

Introduction

1.1 Physics with Heavy Ion Collisions

In the standard model of particle physics, nucleons are constituted of quarks and gluons. Each flavor of quark comes in three colors: red, blue, and green. The strong interactions of quarks and gluons are described by Quantum Chromo Dynamics (QCD), a local $SU(3)$ gauge theory. Quarks are confined into hadrons by the color face and can not be observed as naked particles. The interaction between quarks becomes weak in the large momentum transfer. The properties of quarks confined have been investigated in high energy experiments. For example, the proton structure function in deep inelastic scattering measured at the HERA ep collider at DESY. The quark density increase enormously at very small values of momentum fraction [1].

The field of ultra-relativistic heavy ion collisions combines the elementary interaction aspect of high energy particle physics with the macroscopic matter aspect of nuclear physics. It is focused on the investigation of the properties of nuclear bulk matter made up of strongly interacting particles, i.e. hadrons, quarks, and gluons.

There have been many experiments performed with ultra relativistic heavy ion collisions which have been committed to the exploration of nuclear matter under extreme conditions of high temperature and high density. Particular emphasis of the experiments is on the discovery of Quark Gluon Plasma (QGP), which is a new phase of matter where quarks and gluons are de-confined.

The study of deconfined matter is not only relevant for the understanding of heavy ion collisions but also for astrophysics. The QGP phase is expected to have existed in the early universe before about 1$\sim$10 μsec after the Big Bang, a transient stage of strongly interacting matter persisted at temperatures of about 10^{12} K and low baryon density. Fig. 1.1 shows the a schematic diagram of hadronic matter [2]. The vertical axis is the temperature and horizontal axis is the baryon density. The theoretical aspects are summarized in [3]

1.2 Chiral Symmetry Restoration

In the limit of vanishing quark mass, the QCD Lagrangian proves additional symmetries. It is invariant under global vector λ^b and axial-vector $\lambda^b\gamma^5$ transformations in flavor space:

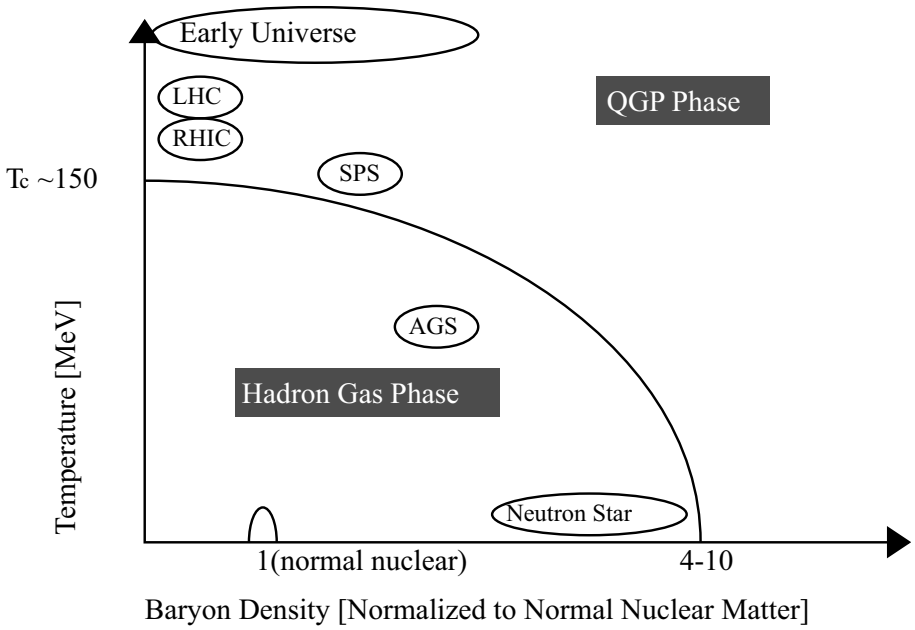

Figure 1.1: Phase diagram of hadronic matter. The emerging picture of the transition from hadronic to quark matter is illustrated.

$$\psi_q \to \exp(-(i/2)\lambda^b \alpha_R^b)\psi_q \quad \text{and} \quad \psi_q \to \exp(-(i/2)\lambda^b \alpha_A^b \gamma^5)\psi_q \tag{1.1}$$

with parameters α_R^b and α_L^b being arbitrary vectors in flavor space. With the quark-spinor projection of right- and left- handed components:

$$\psi_{R/L} = \frac{1}{2}(1 \pm \gamma^5)\psi_q, \tag{1.2}$$

the global vector λ^b and axial-vector $\lambda^b\gamma^5$ transformation can be written as:

$$\psi_R \to \exp(-(i/2)\lambda^b \alpha_R^b)\psi_R, \quad \psi_L \to \psi_L, \tag{1.3}$$
$$\psi_L \to \exp(-(i/2)\lambda^b \alpha_L^b)\psi_L, \quad \psi_R \to \psi_R, \tag{1.4}$$

This describes a global $\mathrm{SU}(3)_R \times \mathrm{SU}(3)_L$ chiral symmetry in flavor space [6]. Left and right handed quarks are not mixed dynamically.

In the normal condition, chiral symmetry seems to be broken. For example, a large mass splitting is shown as the chiral partners such as $\rho(770)$ and $\mathrm{a}_1(1260)$. Then, the ground state, i.e. the QCD vacuum, is not invariant under chiral transformation.

The strength of the symmetry breaking can be characterized by the expectation value of the so-called chiral condensate $< \bar{\psi}\psi >$:

$$< \bar{\psi}\psi >=< 0|\bar{\psi_L}\psi_R + \bar{\psi_R}\psi_L|0 > \tag{1.5}$$

This is the lowest dimensional order parameter charactering the chiral phase transition. The chiral condensate vanishes in the chiral symmetric phase but becomes finite in the asymmetric phase. It is expected that a transition from the asymmetric phase to a phase where the chiral symmetry is restored can be triggered by external parameters such as temperature and pressure. In the QGP phase, it is expected that the chiral condensate vanishes and chiral symmetry is restored by a melting of the quark condensate [5]. During the phase transition, the quarks are expected to lose their constituent mass that leads to the restoration of chiral symmetry. Left and right handed quarks are expected to decouple and hadronic states of opposite parity become degenerate [6]. Particularly, if chiral symmetry restoration is occurred, mass of light vector mesons (ρ,ω,ϕ) are expected to be shifted.

Many signatures (J/ψ suppression [7], direct photons [8] etc..) have been proposed to search the new phase of matter. Among those signatures, low mass dileptons stand out as significant measurement at QGP searching. Because dileptons couple directly to vector mesons and suffer minimal final state interaction with interacting only electromagnetically. Then, hadronic process are expected to reveal their properties in dilepton (vector meson) spectra. The ρ meson has special importance, because once produced in a dense and hot hadronic environment, it will decay predominantly within the fireball due to its short life time. This phenomena is observed with such light vector mesons, as one of the signature of the existence of QGP phase in heavy ion collision.

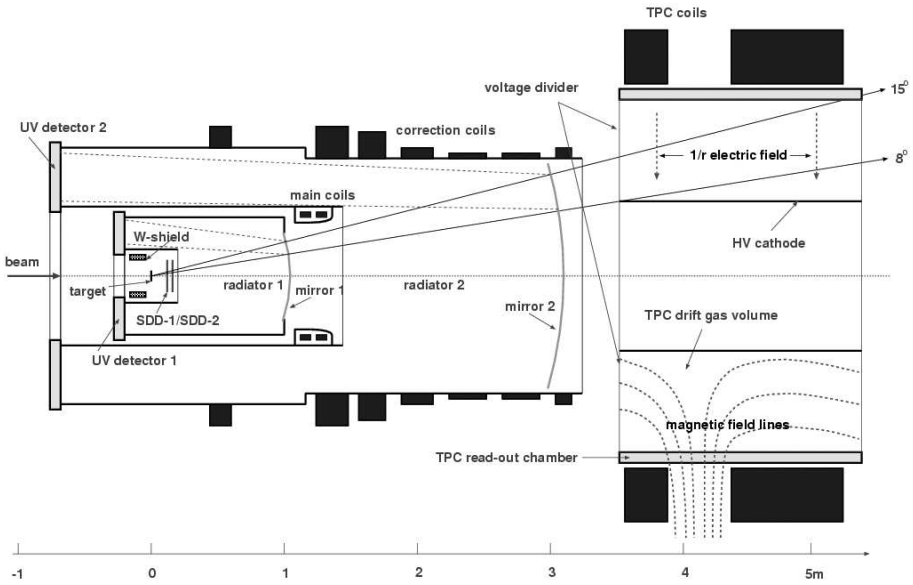

Figure 1.2: Schematic view of the CERES setup used for the measurement of Pb-Au collisions. In order to determine particle momentum, a magnetic field of 7 T was produced between RICH-1 and RICH-2 detector.

1.2.1 The CERES/NA45 Experiment

The low-mass electron pair production in 158 AGeV/c Pb-Au collisions was investigated with the Cherenkov Ring Electron Spectrometer (CERES). This experiment was held at the Super Proton Synchrotron accelerator (SPS) at CERN to search for modifications of hadron properties in hot and dense nuclear matter.

Fig. 1.2 shows the setup of CERES experiment. This experiment was designed to measure di-electron with invariant mass up to 2.0GeV/c^2, covering a pseudo-rapidity range of $2.1 < \eta < 2.65$. The setup of the CERES experiment consisted of two Ring Imaging Cherenkov detectors (RICH) and a large cylindrical Time Projection Chamber (TPC). The RICH detector was expected to provide electron identification and to determine particle momentum. A magnetic field of 7 T was produced between RICH-1 and RICH-2 detector to determine particle momentum. Fig. 1.2 shows the particular field shape. Charged particles that cross this increasing magnetic field (B $\sim$ 1/r) are azimuthally deflected by an angle $\Delta\phi$. The momentum value was obtained from this $\Delta\phi$ value as following relation:

$$\Delta\phi \approx \frac{144 \text{ mrad}}{p \text{ GeV}/c} \tag{1.6}$$

TPC was expected to make the high precision momentum measurement and the considerable reduction of the combinatorial background from the additional dE/dx measurement [9].

Figure 1.3 shows a result of CERES experiment [10]. Left figure in Fig. 1.3 shows the result from 450 A GeV/c p-Au collision. pA data was used as a reference for the evaluation of nucleous-nucleous collision. The hadronic cocktail accounts for the measured di-electron yield.

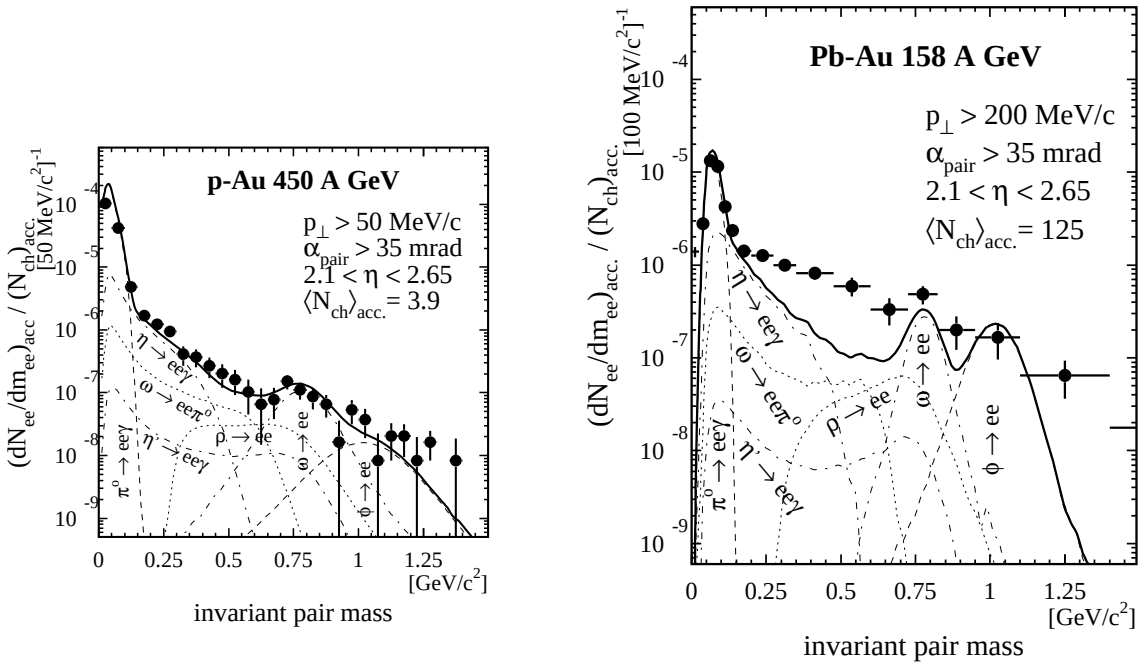

Figure 1.3: Invariant mass spectra at CERES Experiment. Left figure shows the result from 450 A GeV/c p-Au collision. Right figure shows the result from 158 A GeV/c Pb-Au collision data recorded in 1996. The di-electron yield in the mass range of $0.25 < m_{ee} < 2$ GeV/c exceeds the expectations extrapolated from p-p collisions [11].

The hadronic cocktail means the simulation which is based on the branching ratios and the total production cross sections measured in p-p collisions.

Right figure shows the result from 158 A GeV/c Pb-Au collision data recorded in 1996. The di-electron yield in the mass range of $0.25 < m_{ee} < 2$ GeV/c exceeds the expectations extrapolated from p-p collisions [11]. This result is may be an evidence of the chiral symmetry restoration and deconfinement.

1.2.2 The PHENIX Experiment

The PHENIX [12, 13] detector system is a complex of spectrometers to measure hadrons, photons, electrons and muons. Fig. 1.4 shows the schematic layout of the PHENIX setup. It consists of two central arms, two muon arms, and inner detector for event characterization. The detector system was made for study of hot and dense nuclear matter, produced by Au+Au collisions at $\sqrt{s_{NN}} = 200$ AGeV at the Relativistic Heavy Ion Collider (RHIC) in Brookhaven National Laboratory (BNL).

In order to study QCD at high density the PHENIX experiment was specifically designed to detect penetrating probes: electromagnetic radiation and hard scattering processes. In addition, di-electron is proposed as one of the observable in the searching for the restoration of chiral symmetry in the QGP phase. As shown in above section, CERES experiments demonstrated

the unique physics potential of the mass shift of low mass dileptons. To identify electrons, there is a Ring Imaging CHerenkov (RICH) detector at the PHENIX setup. But it is difficult to detect electron pairs from vector mesons because of huge combinatorial background. The large background are primarily coming from γ conversions and π^0 Dalitz decays. Also, the contribution from the open charm ($D \rightarrow \mu, e + X$) is considerable for background rejection. The present setup dose not allow an efficient measurement of low-mass electron pairs in the mass region $m_{e^+e^-} \leq 1$ GeV/c^2. Actually, the first results of PHENIX experiment show that the ϕ meson detected with a signal to background ratio as small as 1/20 [14], making impossible a high quality measurement of the low mass dileptons.

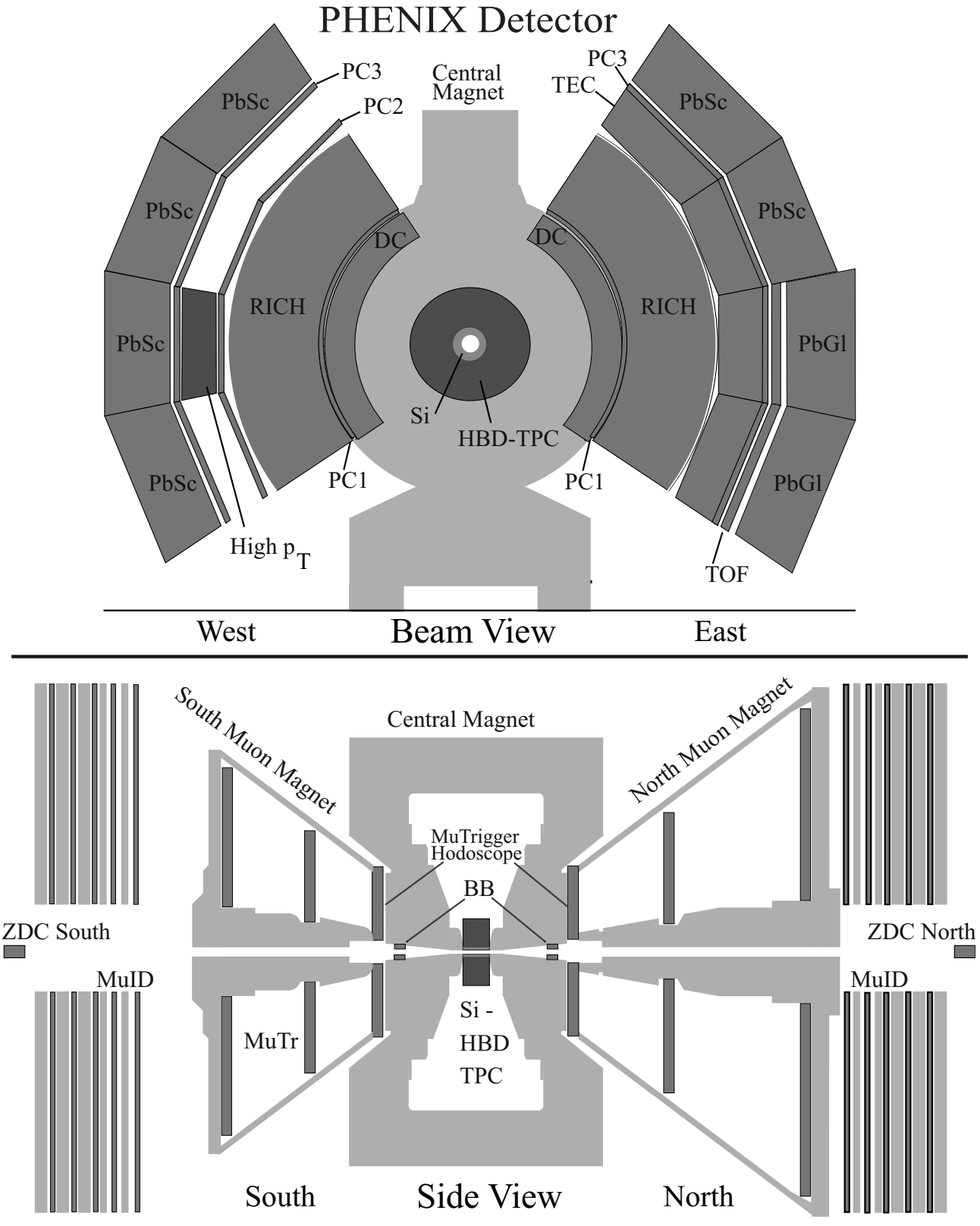

Figure 1.4: Layout of PHENIX detector with possible upgrades. This system consists of two central arms (East and West), two muon arms (North and South), and inner detector for event characterization.

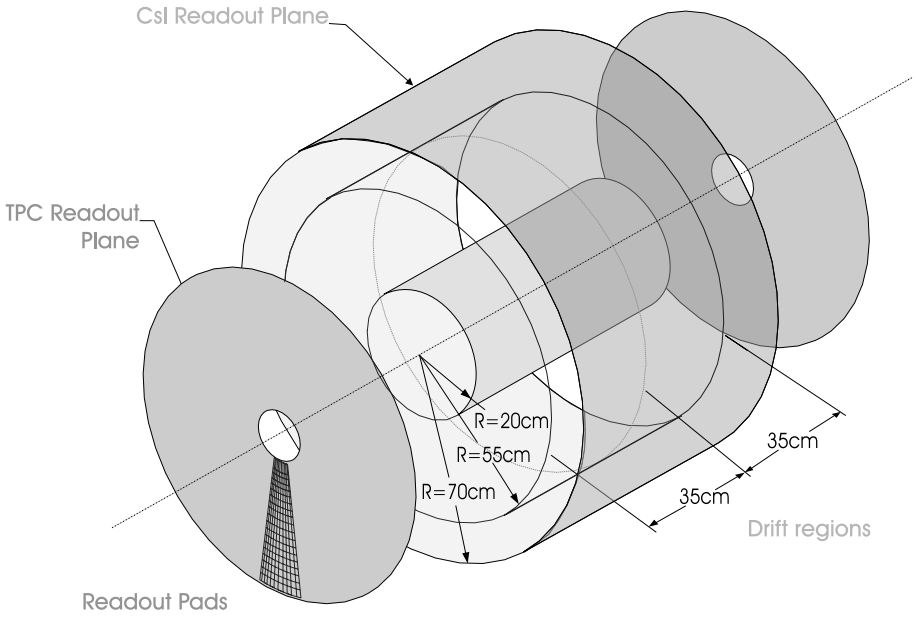

Figure 1.5: Conceptual design of the TPCHBD detector for PHENIX. TPC/HBD consists of two types of detectors; one is the Time Projection Chamber (TPC) [15] and another is the Hadron Blind Detector (HBD). The TPC will use the HBD radiator as an ionization gas volume.

1.2.3 PHENIX Upgrade Plan

An appropriate upgrade is needed to identify and reject the background described above. The main strategy is to identify electrons in a field free region and reject the γ conversions and π^0 Dalitz decay pairs exploiting the small opening angle of these pairs. The installation of an inner coil which would create an nearly field free region extending out to 50-60 cm in the radial direction has recently been installed in the PHENIX detector. In addition to this coil, a new vertex spectrometer which has a large acceptance in the pseudo-rapidity $|\eta| \leq 0.50$ and will fulfill the electron identification and rejection tasks is needed.

In order to achieve the electron identification for $p_T < 1$ GeV/c with a sufficient Dalitz rejection power over the full azimuthal angles, installation of the "TPC/HBD" has been proposed. TPC/HBD consists of two types of detectors; one is the Time Projection Chamber (TPC) [15] and another is the Hadron Blind Detector (HBD). The role of TPC and HBD are inner tracker and Dalitz rejector. Figure 1.5 shows a schematic view of the TPC/HBD detector. The HBD is a Cherenkov detector that utilizes CF_4 gas radiator with good transparency for UV photon and CsI photocathode to detect Cherenkov light from electrons with high efficiency, while having very low sensitivity to charged hadrons. The TPC acts as a tracking device, and make associations with Cherenkov light hits in the HBD. The TPC will use the HBD radiator as an ionization gas volume. Electrons generated in this region would be drifted over the distance of 35 cm to readout planes on both end caps of the detector. The TPC would provide an electron identification for p_T <200 MeV/c with dE/dx measurements. The improved invariant mass resolution due to the high precision tracking and electron identification capability of the TPC

will be useful for efficient Dalitz rejection. Higher performance in vertex determination and in momentum reconstruction are also expected.

1.3 Scope of This Report

Development of a prototype TPC for experiments with ultra-relativistic heavy ion collision will be discussed in this thesis. The results that obtained from gas test and beam test at KEK will be shown in this thesis. The contents of this thesis is as follows.

chapter2 The proposals of this TPC is described in this chapter. Reasons why CF_4 is proposed as this TPC gas is explained.

chapter3 The details of the developed prototype TPC and the frontend electronics is explained.

chapter4 Measurements of the basic characteristics of CF_4 gas are described.

chapter5 Beam test was carried out for the evaluation of this TPC. Total performances of the prototype TPC with CF_4 gas are shown.

Chapter 2

Time Projection Chamber for Heavy Ion Collision

2.1 Overview

Time Projection Chamber (TPC) is essentially a three-dimensional tracking detector capable of providing information on many spatial points along a particle trajectory. TPC makes use of ideas from both the multi-wire proportional chamber and the drift chamber. Its basic structure is sketched in Fig. 2.1. TPC is essentially a large gas filled box, or cylinder, with a high voltage electrode at the opposite side of the readout wire. The end of the box are covered by MWPC type readout, arrays of anode wires. With a uniform electric field directed to the anode wire, all electrons created in the sensitive volume of TPC drift towards the end cap chamber. And each anode wire over which the particle trajectory crosses samples that portion of the track. Then the coordinates along the anode wires is given by the position of the readout pads. And the coordinate along the drift axis is given by the drift time of ionization electrons. Many space points for each track can allow a full reconstruction of the particle trajectory.

TPC has played an essential role in several physics experiments including the recent heavy ion experiments. TPC is a central tracking device at the STAR experiment (RHIC in BNL) and at the ALICE experiment (LHC in CERN). New type of TPC is required for higher multiplicity and to be installed at closer position to vertex. Here, the good double track separation capability is required for the TPC in addition to the good position resolution.

2.2 Gas Selection for TPC

2.2.1 Requirements for TPC Gas

Particle multiplicity is very large in heavy ion collisions. One of the requirements for the TPC is capability of good spatial separation between adjacent tracks. Because of the relatively long drift distance, diffusion becomes a mean source of limitation of double track separation. Therefore, gas with small diffusion constant is favorable.

Another requirement is that the drift velocity should be faster than 5 - 10 cm/μsec in order

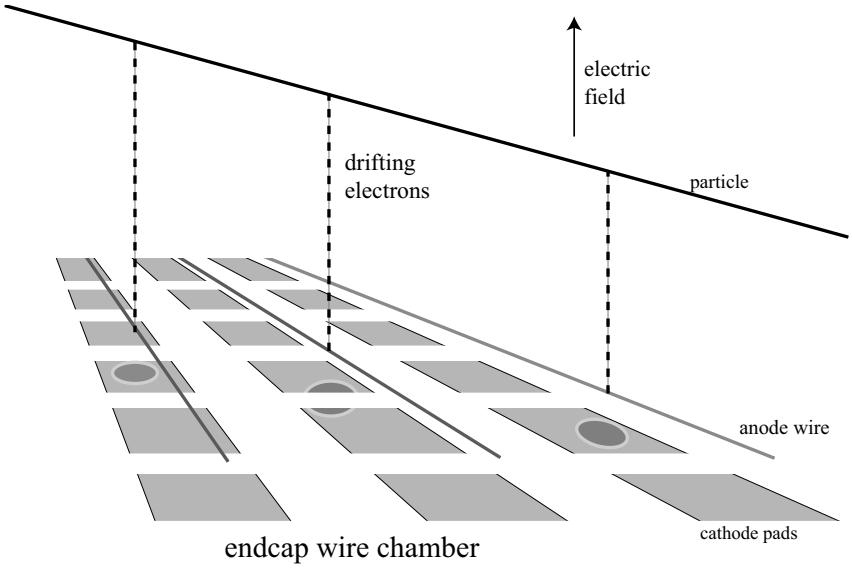

Figure 2.1: Schematic diagram of Time Projection Chamber. With a uniform electric field directed to the anode wire, all electrons created in the sensitive volume of TPC drift towards the end cap chamber. Each anode wire samples that portion of the track. Then the coordinates along the anode wires is given by the position of the readout pads. And the coordinate along the drift axis is given by the drift time of ionization electrons.

to detect two events separately for p+p and light ion collisions for RHIC experiment. Therefore the ionization gas must have a high drift velocity and low diffusion in order to provide both the speed and spatial resolution required for operating in both a high rate and high multiplicity environment.

Some of the candidates of chamber gas which has small diffusion constant are CO_2 mixture and isobutane mixture gases. For example, the longitudinal diffusion coefficients of Ar(70%)-CO_2(30%) and Ar(50%)-isobutane(50%) are 150 μm and 180 μm for 1 cm drift when the electric field is 1000 V/cm, respectively. The choice of CO_2 is often forbidden by the poor quenching properties of this gas in proportional counters and the quoted isobutane mixture is often preferred.

2.2.2 CF_4 Gas

CF_4 was chosen as a candidate for the TPC gas. In CF_4, the drift velocity of electron is about 10 cm/μsec, when the electric field of more than 1 kV/cm is applied. The longitudinal diffusion is less than 200 μm for 1 cm electron drift at the same condition [16]. CF_4 has very fast drift velocity and very small diffusion coefficient comparing with the other gases that are used as chamber gases.

Figure 2.2 shows electron drift velocity of Ar-CF_4 mixtures in the several proportions [22]. As seen in Fig. 2.2, when CF_4 is mixed with Argon in the proportion of one part to nine, the fastest drift velocity is about 12 cm/μs, which satisfies the RHIC requirement.

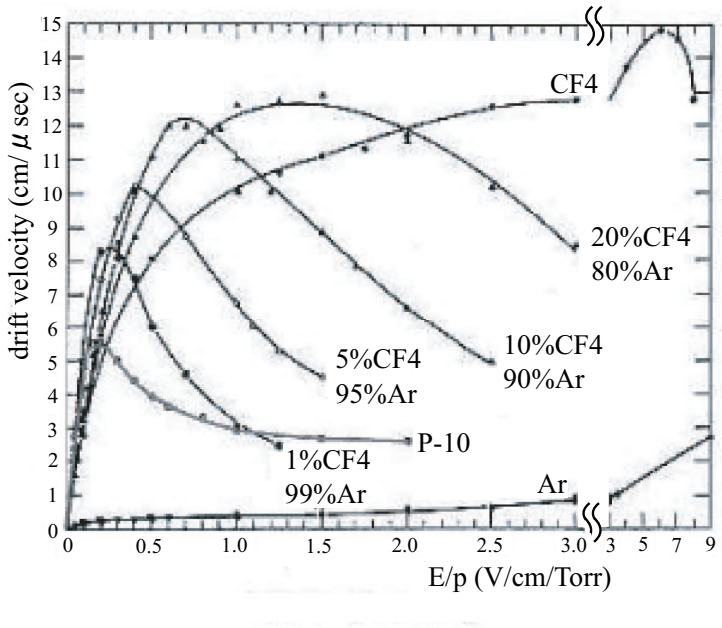

Figure 2.2: Drift velocity of Ar-CF_4 mixtures in the several proportions [22]. The fastest drift velocity is about 12 cm/μs, which is faster than the drift velocity of P10.

2.2.3 Gas Simulation Study

In order to investigate the basic characteristics of CF_4 gas, drift velocity, diffusion, and Townsend coefficient of CF_4 gas was simulated. These characteristics were obtained from Magboltz [17] and Heed [28] simulation. Magboltz solves the Boltzmann transport equations for electrons in gas, and calculate the electron drift velocity, diffusion, Townsend and attachment coefficient for nearly arbitrary gas mixture. The Heed program takes care of electron clustering that is originated from the energy loss through ionization of a particle that transverses the gas.

Figure 2.3 shows the simulation result, transverse diffusion and longitudinal diffusion, function of electric field. This figure implies the longitudinal and transverse diffusion is less than 100 μm for 1 cm drift, when the electric field is more than 500 V/cm.

Figure 2.4 shows the longitudinal diffusion of Ar-CF_4 mixtures as a function of electric field, obtained from Magboltz simulation. Diffusion constants of CF_4 mixtures are much smaller than that of pure Argon and P10. Ar-CF_4 mixtures fulfills the both requirements for two particle separation and for two events separation.

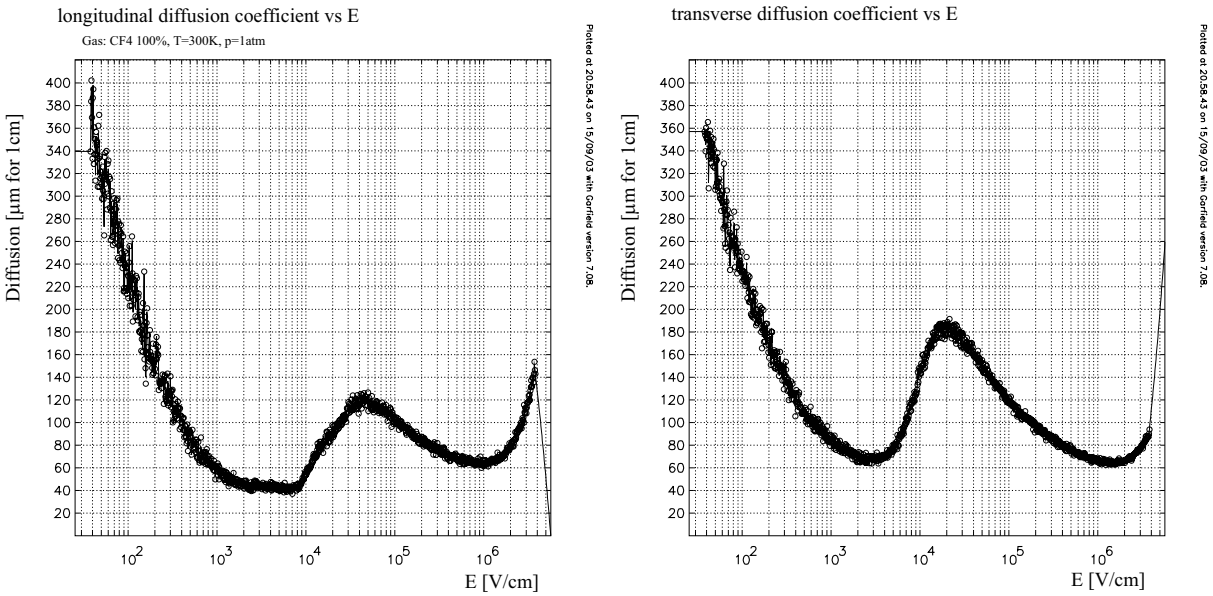

Figure 2.3: Diffusion coefficient of pure CF_4 from simulation. The longitudinal and transverse diffusion is less than 100 μm for 1 cm drift, when the electric field is more than 500 V/cm.

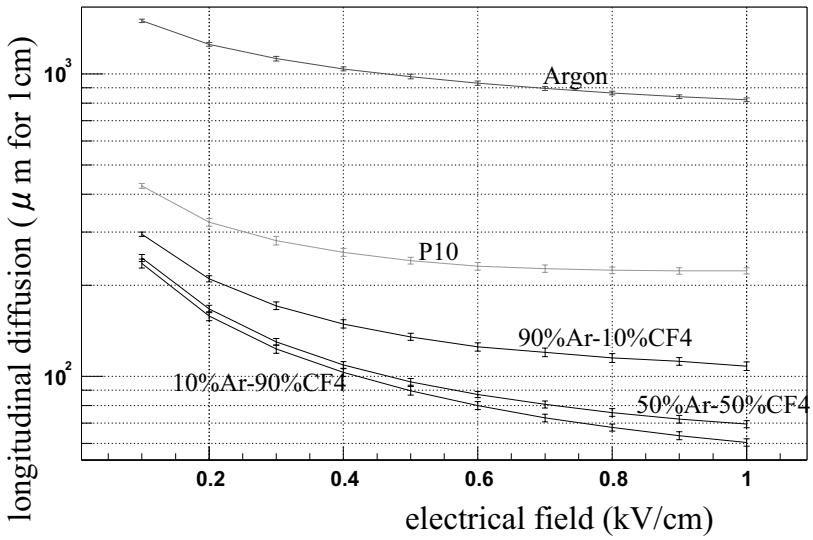

Figure 2.4: Longitudinal diffusion of Ar-CF_4 mixtures, pure Argon, and P10. Diffusion constants of CF_4 mixtures are much smaller than that of pure Argon and P10.

Chapter 3

Prototype TPC

In order to investigate the characteristics of CF_4 gas and the tracking capabilities with CF_4 gas, a prototype TPC was developed. In this chapter, details of the prototype TPC is discussed.

3.1 Overview of prototype TPC

The design of a prototype TPC is shown in Fig. 3.1. The dimension of gas vessel is cuboid 29 cm $\times$ 29 cm $\times$ 60 cm, which is made of Aluminum. The thickness of the Aluminum plate used for gas vessel is 3.2 mm $\sim$ 15 mm. This TPC is expected to keep gas purity ($\sim$ 10 ppm - 100 ppm) with flowing the chamber gas. The expectation of gas purity is defined from the actual situation where the PHENIX TPC is expected to be installed. The chamber gas is flowing into the gas vessel though the gas system connected with gas tube made of Teflon. In order to keep the gas tight, the Aluminum plate is bonded each other using rubber ring or rubber cement. This TPC is not designed to bear the pressure from vacuum and it's impossible to make gas purity with drawing a vacuum.

The drift cage with dimensions of 16 cm $\times$ 16 cm $\times$ 36 cm made of multistage gold strips on G10 board is installed in the gas vessel. A drift cage is shown at the center of the upper figure of Fig. 3.1. Mechanically, a field cage is composed of two parts, i.e. a top electrode with a high negative voltage supplied and side strips keeping a uniform gradient of the potential in the whole drift region. Field HV is supplied to the top plate of the field cage as shown in the right of the upper figure of Fig. 3.1. To make a gradient of the electric potential, the field strips are connected to each other through a ladder of registers. In order to cover a discharge between the gas vessel and the field cage, the field strips are settled at a distance of 4 cm from the gas vessel. When CF_4 gas is used as the chamber gas, the HV of -31 kV can be applied at the top plate with this condition.

This TPC has the multi-wire proportional chamber (MWPC) type readout that consists of grid wires, anode wires, and cathode pads in the end cap as shown in Fig 3.2. Sensitive volume for trajectory is 10 cm $\times$ 10 cm $\times$ 33 cm. This is determined by the scale of readout and the field cage. Induced signals are readout with cathode pads mounted on the pad plane. 4 types of pads(2.5 mm, 6 mm, 9.5 mm and 13 mm square) are prepared to investigate the performance as a function of the scale of readout pads.

In order to test with a laser beam, 6 quartz windows are opened into the field cage with gap of 15.4 mm.

Calculations were performed to simulate the property of TPC, by using a computer program, Garfield[23], which was developed for the detailed two- and three-dimensional gaseous chambers. With the simulation, the geometrical parameters, for example, length, width and pitch of the strip of the electric field cage, pitch and diameter of anode wire, and size of cathode plane can be optimized.

The frontend electronics for each cathode pad is composed of a pre-amplifier, a signal driver and a flash analog-to-digital converter (FADC) sampling the driven signals. In order to detect the double tracks with good resolution, fast sampling type ADC is used and a new type of pre-amplifier is developed.

Following section discusses the details of such part.

3.2 Field cage

One of the requirements to the prototype is that it is possible to apply drift field of more than 900 V/cm in order to test the performance of CF_4 gas. The effective total length of the drift region is about 33 cm. As shown in Fig. 3.2 the drift field is determined by the HV applied to the top plate($\sim$ -30 kV). The field cage has 4 mm wide field strips with gaps of 2 mm between adjacent strips, printed on both sides of the side walls of its cage, 1.6 mm thick plates of glass epoxy (G10). The field strips are connected to each other through a register. The ladder of registers consists of 116 registers of 1 MΩ each. It leads to the bias current of $\sim$ 270 μA when the HV of -30 kV is applied to the top plate. The maximum drift field is typically 900 V/cm. This is limited by the -30 kV power supply limit.

A simulated result of electric field in the drift region is shown in Fig. 3.3. The upper figure shows the potentials of the field, and the lower figure shows the drift line of the electron generated by incident particle. GARFIELD is used for this simulation and the geometry of the simulated detector is almost same as real detector except for the strips. GARFIELD can not simulate strips and it is simulated as the bunch of the wires. In design of a field cage, the most critical criterion is the uniformity of the inside electric field. Since the maximum drift length of an electron is 33 cm, an inclination of the electric field $E_\perp/E_x$ of 10^{-3} corresponds to a shift of 330 μm of the measured position at worst. $E_\perp$ is electric field perpendicular to the drift direction, and E_x is one in the drift direction. In consideration of effect from the transverse diffusion (80 μm for 1 cm drift), I set the criterion of a tolerable inclination at the value above, i.e.

$$E_\perp/E_x \leq 10^{-3} \tag{3.1}$$

Fig. 3.4 shows the inclination of the electric field $E_\perp/E_x$ of 10^{-3} as a function of the position along the wire direction. x=0 indicates the center of the field cage. The inclination is less than 10^{-3} at $|x| \leq 6$ cm. This field cage satisfy the criteria for drift electrons detected at the readout whose scale is about 10 cm square.

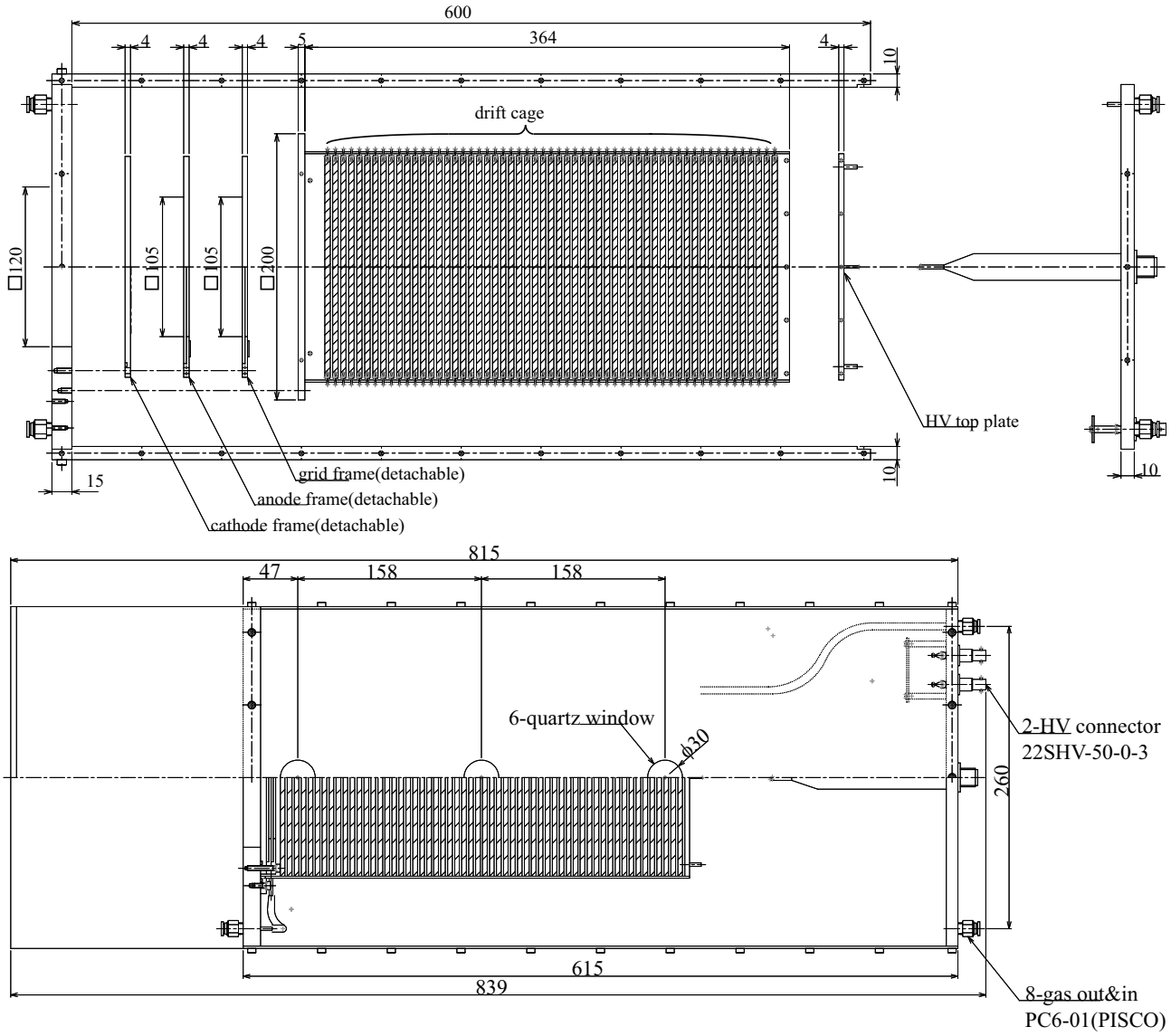

Figure 3.1: Design of prototype TPC. The dimension of gas vessel is cuboid 29 cm × 29 cm × 60 cm, which is made of Aluminum. The drift cage with dimensions of 16 cm × 16 cm × 36 cm made of gold strips on G10 board is installed in the gas vessel. The large HV connector shown at the right is used for field cage power supply. The left end cap is MWPC type readout. The lower figure is the side view of prototype TPC. 6-quartz windows are opened for gas test with laser beam. 2-HV connectors are used for HV to anode and grid wires. There are 8-gas connectors to connect gas system.

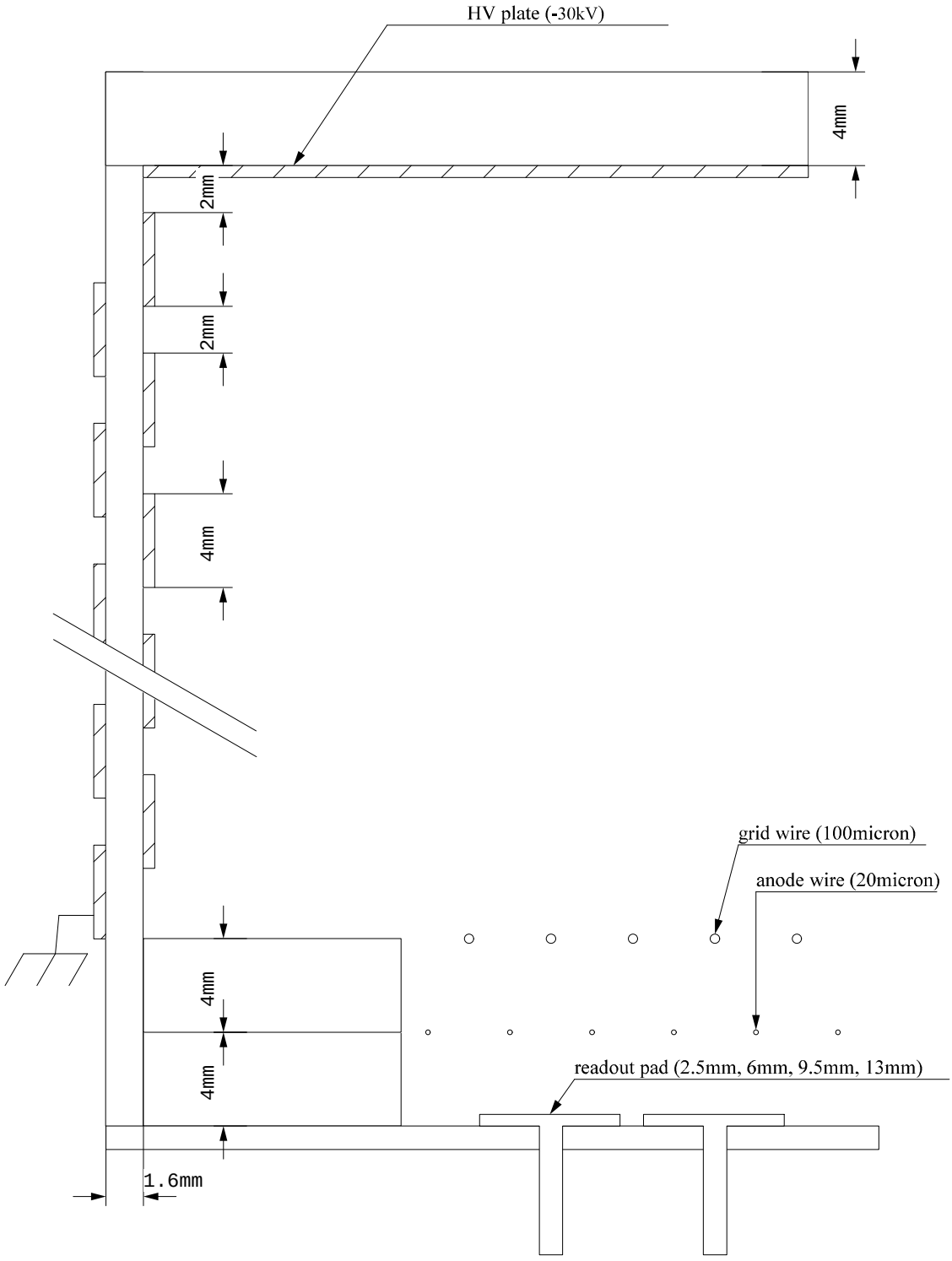

Figure 3.2: A brief cross section view of field cage and readout region. The drift field is determined by the HV applied to the top plate($\sim$ -30 kV). The field cage has 4 mm wide field strips with gaps of 2 mm between adjacent strips, printed on both sides of the side walls of its cage, 1.6 mm thick plates of G10. The field strips are connected to each other through a 1 MΩ register. This TPC has the MWPC type readout that consists of grid wires, anode wires, and cathode pads in the end cap with 3.5 mm wire spacing and 4 mm

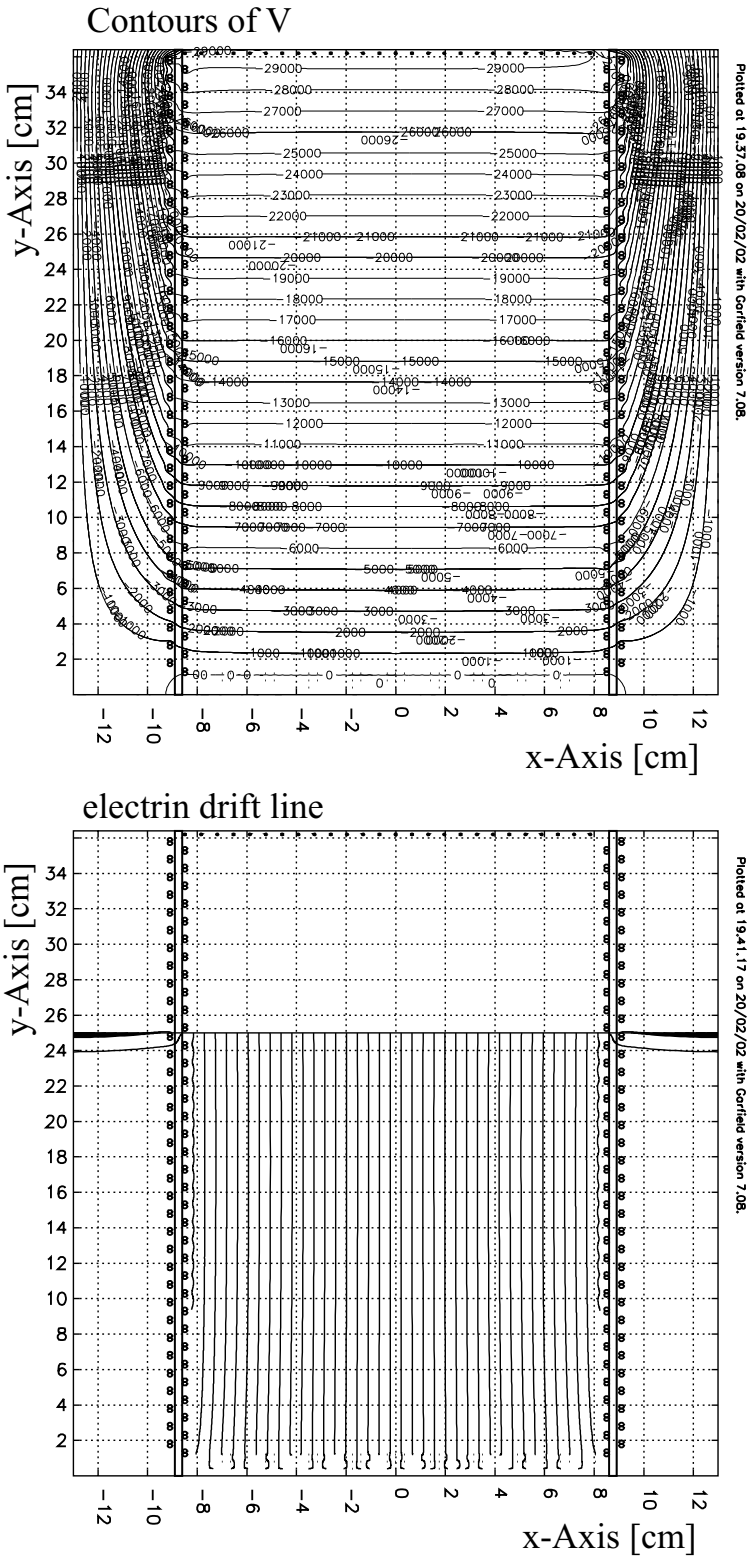

Figure 3.3: Electrical field constituted by field cage. The upper figure shows the contours of electric potential. The lower figure shows the electron drift line when a muon of 10 GeV/c incidents at y=25 cm.

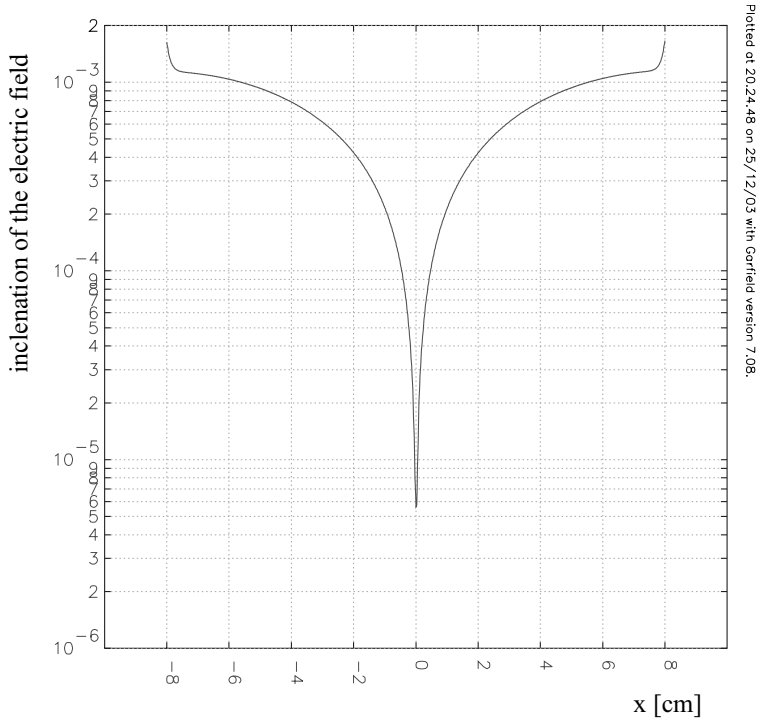

Figure 3.4: An inclination of the electric field $E_\perp/E_x$ at y=10 cm in Fig. 3.3 as a function of the position along the wire direction when x=0 indicates the center of the field cage. $E_\perp$ is electric field perpendicular to the drift direction, and E_x is one in the drift direction.

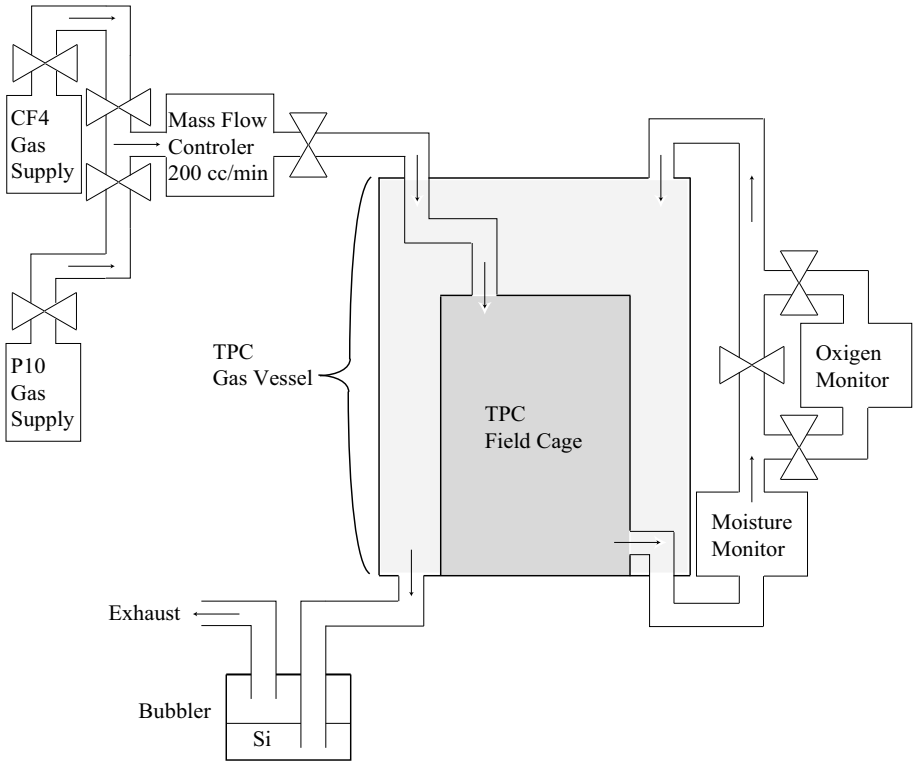

Figure 3.5: A schematic view of the gas system for the prototype TPC. This gas system consists of a mass flow controller(ESTEC Co. Ltd., SEC-E40), moisture monitor(PANAMETRICS Co. Ltd., Moisture Monitor Series 35 IS), oxygen monitor(DELTA F Co., FAH0100S) and bubbler mainly.

3.3 Gas system

A gas system was constructed to supply pure CF_4 and P10 to the prototype TPC. Figure 3.5 shows a schematic view of the gas system. The gas system consists of a mass flow controller, moisture monitor, oxygen monitor and bubbler mainly. The mass flow controller (ESTEC Co. Ltd., SEC-E40) is used to control the rate of flowing in this gas system. The moisture monitor (PANAMETRICS Co. Ltd., Moisture Monitor Series 35 IS) and the oxygen monitor (DELTA F Co., FAH0100S) are used to monitor how much electro-negative gases are contained in the flowing gas. In order to monitor the flowing gas from the field cage, the moisture monitor and oxygen monitor are placed at the just down stream of the field cage. Oxygen is not monitored at any time, because it suppresses the rate of gas flowing. The bubbler is placed at the most down stream of the gas system not to flow upstream.

As shown in Fig. 3.1, the field cage of the prototype TPC is in the TPC gas vessel. In order to use the gas as pure as possible, input gas flows into the TPC field cage at first. And the gas flows into the gas vessel which surrounded the field cage after the gas goes through the moisture monitor.

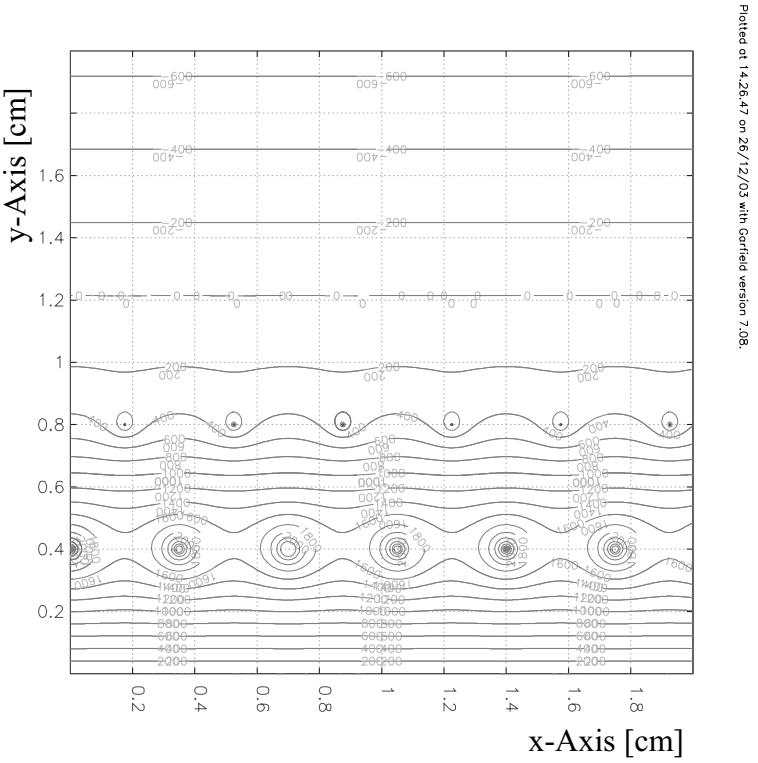

Figure 3.6: Contour of electric potential around the readout. The electric field of the proportional region is protected from the drift field.

3.4 Readout

The end cap wire chamber consists of three layers, i.e. grid wires, anode wires, and a cathode pads, from the top to the bottom with 3.5 mm wire spacing and 4 mm gaps between the layers. The spacing of the anode wires of 3.5 mm is fixed based on the requirements that cathode pads of 2.5 mm square are used as readout pad with 1 mm gaps. The spacing of the grid wires are determined to assure that the drift field does not affect the electric field in the readout region. Figure 3.6 shows the contour of electric potential around the anode wire. The electric field of the proportional region is protected from the drift field. The gap width of 4 mm is one of the standard values for this kind of chambers. Quantity of the positive ion feedback in this placement is estimated as shown in Fig. 3.7. About 5 % positive ions generated from avalanches are expected to drift into the drift field, if ionization avalanches spread around the anode wires isotropically. In the P10, the spread of avalanches on a anode wire occupies only 100 ° in azimuth (FWHM) in the readout [24]. Then, about 5 % $\times$ 360/100 = 18 % positive ions generated from avalanches are expected to drift into the drift field in this geometry.

To achieve a high enough gas gain at a relatively low operating voltage, thinner anode wires are preferable. Since it is difficult to handle wires thinner than 10 μm in diameter, gold-plated tungsten wires of 20 μm are chosen for the anode wires. For the grid wires, gold-plated tungsten wires of 100 μm are used.

The induced charge is readout from cathode pads as electron signals. At the bottom of

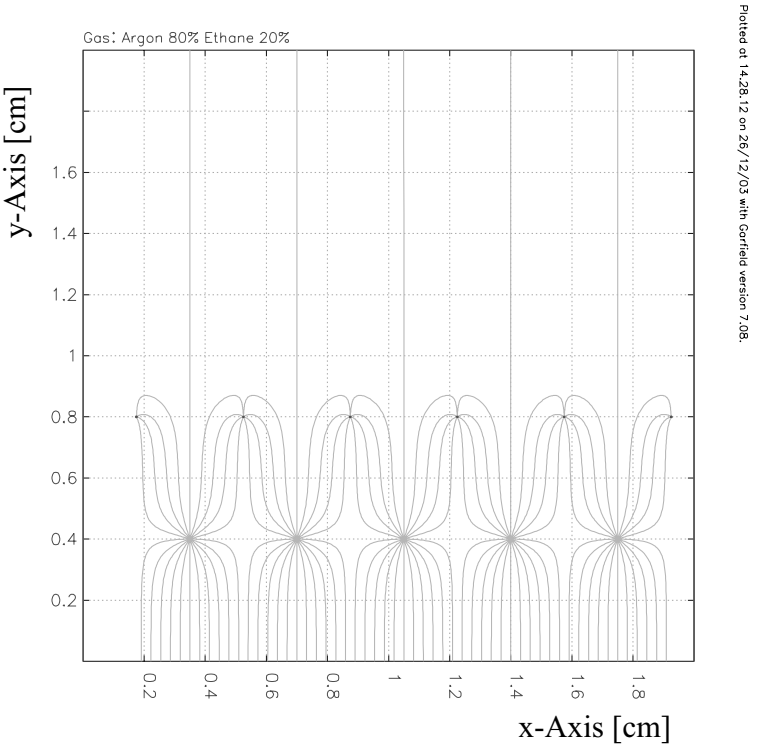

Figure 3.7: Ion drift lines from anode wires.

the readout, connectors for pre-amplifiers are attached. Details of the pre-amplifier will be discussed at the following section. The anode signals are not read out. In order to protect the anode wires from a noise from the HV supply, a simple low pass filter is used.

In order to evaluate the position resolution as a function of the scale of the cathode pads, four different size of cathode pads were prepared with 1 mm gaps between the pads; 2.5 mm, 6 mm, 9.5 mm, and 13 mm square, as shown in Fig. 3.8.

The scale of the cathode pads, 2.5 mm, 6 mm, 9.5 mm, and 13 mm, is decided from the three factors. One is the capacitance between cathode and TPC detector. In order to detect the induced signal precisely, the capacitance should be small compared with the one which determines the open loop gain of the pre-amplifier. The signal cannot be measured precisely when it is too big to hold the linearity of the signal gain. Other factor is the dimension of the pads to collect the induced charge enough to allow the FEE to reach a reasonable S/N ratio in order to detect the signals. The reasonable S/N ratio is estimated about 20. The pads whose dimension is smaller than 1.5 mm square is too small to collect the signals with reasonable S/N ratio in this system. Other factor is the distribution of the induced charge on the cathode pads to archive the required resolution with this TPC. The surface charge density $\sigma(x)$ on anode wire is estimated using the method of image. Since the distance between grid and cathode is 8 mm in this case, the total charge density is obtained as follows:

$$\sigma(x) = -\frac{1}{8\cosh(\pi x/8)} \tag{3.2}$$

where, x is position along to the anode wire when a drift electron was collected at x=0. If an error of 0.4 % are assumed for the measured pulse heights, the position error is about 50 μm for 6 mm readout strips. The influence of transverse diffusion of the chamber gas is neglected in this estimation.

Figure 3.9 shows the induced current from a cathode pad calculated with GARFIELD for several different pad sizes when the chamber gas is Argon (80 %)-C_2H_6 (20 %). The larger pads can detect the larger induced currents. For pure CF_4, a net signal is simulated as shown in Fig. 3.10. The expected rise time of a signal is about 30 nsec. The rise time is defined by largeness of electron cloud and depends on the readout geometry (pitch of the anode wires).

The readout is detachable for testing with other type of readout. The pads and wires are mounted in each frames shown as 4 mm plate at the left of the upper figure of Fig. 3.1. A idea about readout is gaseous charge amplification with Gas Electron Multiplier (GEM)[19]. GEM is a metal-clad polymer foil with holes. By applying voltage to the metal layers of a GEM, a drift electron passing through the hole causes a avalanche by an application of a difference of potential between the two electrodes, which are transferred and collected by readout system. Gains of the order of 10^6 can be realized with triple-GEM configuration by applying relatively low voltage compared with typical wire chambers.

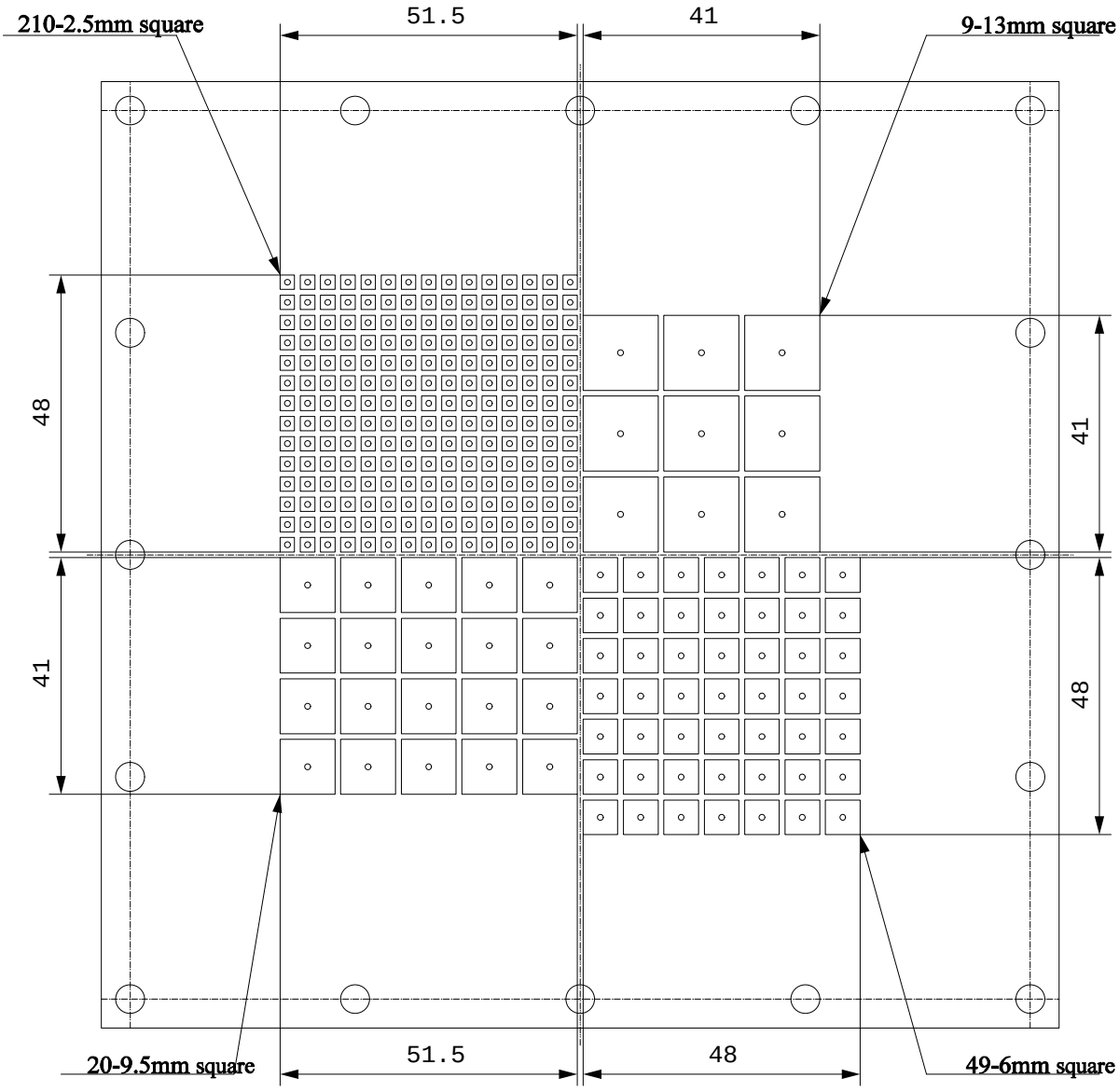

Figure 3.8: Geometry of Readout Pads. Four different size of cathode pads were prepared with 1 mm gaps; 2.5 mm, 6 mm, 9.5 mm, and 13 mm square.

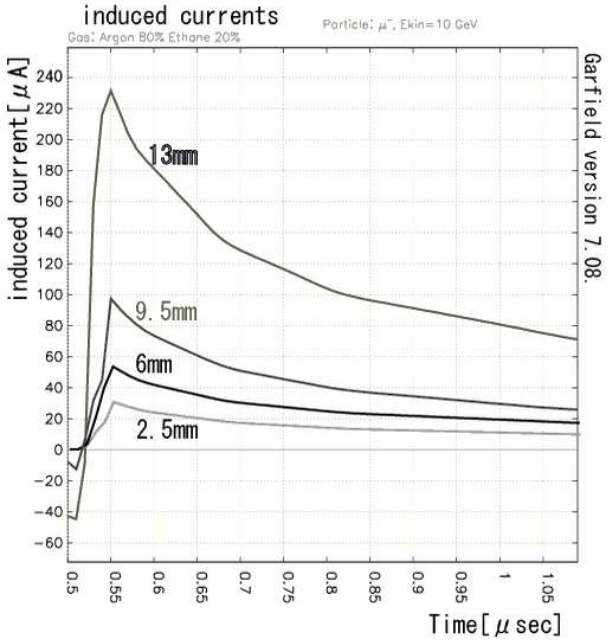

Figure 3.9: Induced current for each type of pads (Argon-C_2H_6). With simulating the signals from incident muon with 1 GeV/c, the signal that was expected to be read is calculated for each type of pads. The 2.5 mm, 6 mm, 9,5 mm, and 13 mm in the figure mean the size of pads, 2.5 mm, 6 mm, 9,5 mm, and 13 mm square, respectively.

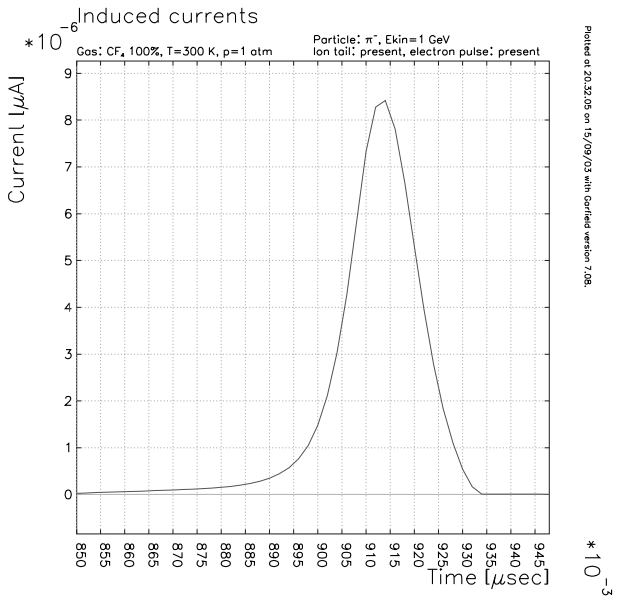

Figure 3.10: Expected induced current with 13 mm square pads (CF_4). The rise time of a signal is about 30 nsec.

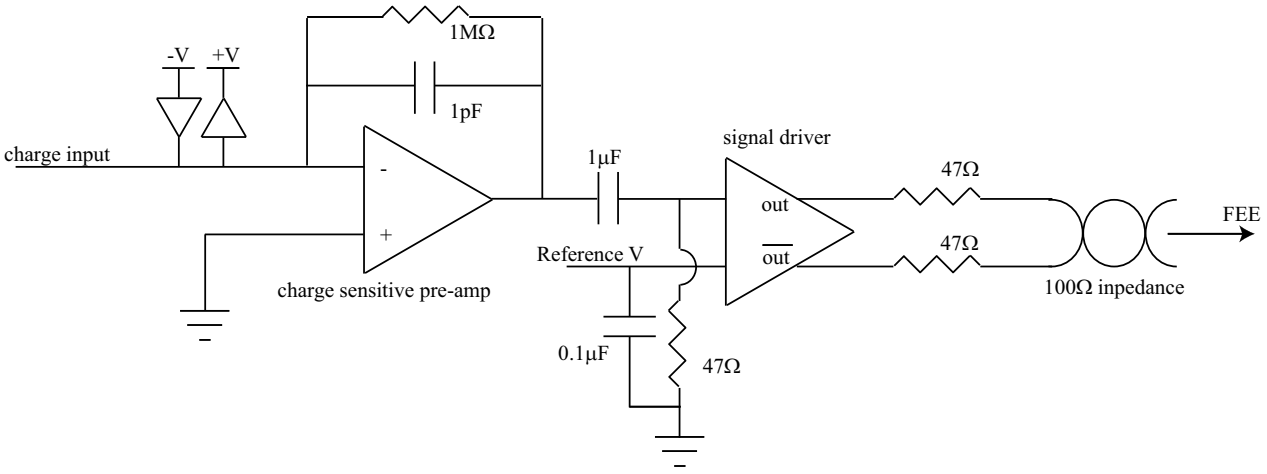

Figure 3.11: Schematic diagram of TPC pre-amplifier. AD8058 opamp (Analog Devices, Inc.) with feedback capacitance of 1 pF and AD8131 opamp (Analog Devices, Inc.) are used for the pre-amplifier and signal driver, respectively. Two diodes are used to protect the opamp from excessive currents. In order to cut the offset from the pre-amplifier, a capacitance of 1 μF is used between two opamps. With AD8131 signal driver, signals are driven though 100 Ω impedance twist cable.

3.5 Pre-Amplifier

Pre-amplifier was developed to convert the charge signal from TPC pads to voltage signal. The pre-amplifier has high gain, 1 V/pC, and large bandwidth for fast signal.

Fig. 3.11 shows the simple circuit diagram of a pre-amplifier board for one channel. This pre-amplifier consists of two main parts, charge sensitive pre-amplifier part and differential signal driver part. AD8058 opamp (Analog Devices, Inc.) and AD8131 opamp (Analog Devices, Inc.) are used for the pre-amplifier and signal driver, respectively. The characteristics of these chips are listed in Table 3.1. Expected bandwidth of this pre-amplifier is 300 MHz.

AD8058 opamp (Analog Devices, Inc.) is used for the pre-amplifier with the feedback capacitance, 1pF. The value of the capacitance was determined in order to make high gain with the lowest noise with keeping amplitude linearity. It was determined to satisfy the following relation:

$$A_{\rm gain} \gg \frac{C_{\rm cathode-detector} + C_{\rm feedback}}{C_{\rm feedback}} \tag{3.3}$$

where, the $A_{\rm gain}$ is open loop gain of the opamp, the $C_{\rm cathode-detector}$ is the capacitance between the readout pad and the detector, and the $C_{\rm feedback}$ is the feedback capacitance. Open-loop gain of the AD8058 is 55 dB and the capacitance between a cathode pad and the detector is 0.085pF when the cathode pad is 13 mm square. In order to make the ratio given by the relation 3.3 less than 0.1 %, the value of feedback capacitance should be more than 0.2 pF.

One of the motivation to develop a new type of pre-amplifier is to make available two track

separation as small as possible. As shown in Fig. 3.9 the expected rise time is 30 nsec. The slew rate of 1000 V/μsec is much faster than the expected rise time of input signals and enough not to make slow the signals. In order to separate double signals with keeping charge information, time constant value is 1 μsec not to decay the input signal. The double tracks are expected to be shown as double rising pulse like steps. A double track signal will be shown at the following beam test section.

Since the input signal to the flash ADC should be a differential one, the pre-amplifier is designed to make differential output signal. The signal noise that may cause while the driving is compensated because of the differential signal driving. AD8131 opamp (Analog Devices, Inc.) is used for the signal driver. The AD8131 is a differential driver for the transmission of high-speed signals over low-cost twisted pair with very low harmonic distortion. This opamp is a differential or single-ended input to differential output driver requiring no external components for a fixed gain of 2.

	AD8058	AD8131
-3 dB Bandwidth	300 MHz	400 MHz
Slew Rate	1000 V/μsec	2000 V/μsec
Input Voltage Noise (20 MHz)	7 nV/$\sqrt{\text{Hz}}$	25 nV/$\sqrt{\text{Hz}}$
Open-Loop gain	55 dB	fixed
Operating Range of Voltage supply	$\pm$6.0 V	$\pm$5.5 V
Quiescent Current	6.0 mA	11.5 mA

Table 3.1: specifications of opamp for the pre-amplifier

3.6 Frontend Electronics

A flash ADC (RPV-160 by REPIC Co., Ltd) module was used for converting to digital information from voltage signals. It has the dynamic range of 8bit (0 $\sim$ -1 V) with 2k words memory for one channel and conversion rate of 100 MHz. The 100 MHz sampling rate is needed for the readout electronics to measure gas characteristics. Because the electron drift velocity is about 10 cm/μs, and the longitudinal diffusion is about 100 μm for 1 cm drift, when the gas is pure CF_4 and the electric field is about $E/p = 1$ (kV/cm/Torr). Therefore the expected rise time of signals are $\sim$20 nsec and more than 100 MHz sampling rate, more than 3-time ADC samples for each signals, is required for the good fitting to determine the electron arrival time. The module is accessed via VME bus ,and the driver to operate the modules was also developed.

This module was used for the measurement of the gas properties (drift velocity, longitudinal diffusion, and attenuation) and for beam test. At the gain measurement, a CAMAC ADC module was used instead of FADC, and details of the CAMAC ADC module will be described at following gas test section.

Chapter 4

Study of Basic Properties of CF_4 Gas

The most important subject to be studied with the prototype TPC is the properties of CF_4 gas. The absolute value of gain, drift velocity, longitudinal diffusion, and attenuation of pure CF_4 (99.999 %) was measured using this test cell. The flow rate of the gas in the chamber was adjusted to about 200 cc/min at atmospheric pressure. P10 gas, which is the mixture of Ar (90 %) and CH_4 (10 %)), was also used for reference purpose. Measurements were carried out with a N_2-laser and a ^{55}Fe radioactive source.

Nitrogen laser (Usho Co. Ltd. YKN-500) was used for drift velocity measurement, longitudinal diffusion measurement and attenuation measurement. Characteristics of this laser device is listed in Table 4.1. Total about a hundred electrons can be generated per laser pulse at a beam focal point in pure CF_4.

wave length	337.1 nm
spectral bandwidth	0.1 nm
repetition rate	1∼10 Hz
pulse width	4∼8 FWHM
pulse energy	2.5 mJ
peak power	600 kW
average power	24 mW
beam size	V5 mm × H20 mm
beam divergence	V4 mrad × H10 mrad

Table 4.1: Characteristics of N_2 laser (Usho YKN-500)

4.1 Gas Gain

4.1.1 Setup

By illuminating 5.9 keV X-rays from a ^{55}Fe radioactive source, the absolute value of gain was measured.

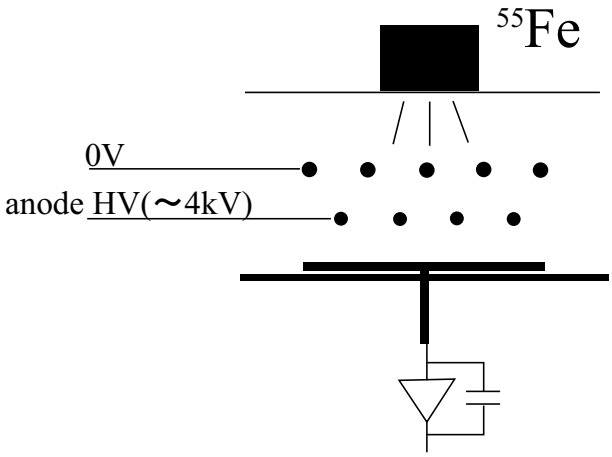

Figure 4.1: A Schematic view of gain measurement. By illuminating the X-ray from a ^{55}Fe radioactive source, about 110 electrons are generated around the anode wire.

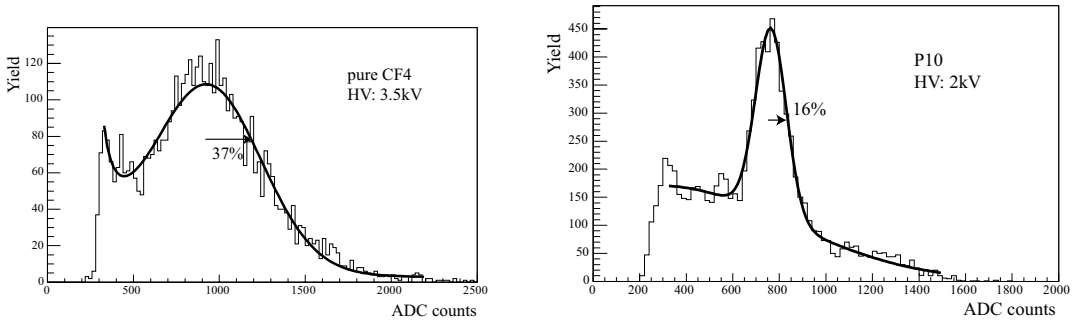

Figure 4.2: ADC spectra of CF_4 and P10. The energy resolution of CF_4 of 37 % is worse than that of P10 of 16 %.

Fig. 4.1 is the layout of setup. A X-ray from the ^{55}Fe radioactive source generates 110 electrons with photoelectric absorption process around the anode wire. The illuminating point was in the middle of active cathode pad of 13 mm square which is large enough to detect almost induced charge.

In order to use large dynamic range, the voltage signals from pre-amplifier are recorded using a CAMAC ADC module (RPC-022 by REPIC Co., Ltd) instead of the flash ADC module in this measurement. The dynamic range of the ADC is 12 bits and the full scale corresponds to 1000 pC. The ADC module is operated using CAMAC controller (PCI7700 by TOYO Co. Ltd.). The KuroDAQ was prepared for DAQ operation. KuroDAQ is Linux base system that uses CERN ROOT library for the analysis.

4.1.2 Test Result

Figure 4.2 shows typical ADC spectra obtained with CF_4 and P10. The energy resolution of CF_4 and P10 were about 37 % and 16 %, respectively. From these distributions the pure CF_4

have poor energy resolution compared to P10. This is most probably due to the production of negative ions (F^-) in the high field region of the chamber via dissociative attachment [25, 26]. Following is a weak ion-pair process in CF_4:

$$CF_4 + e^- \rightarrow F^- + CF_3 \tag{4.1}$$

The poor energy resolution of CF_4 will be appeared as the poor particle identification capability in dE/dX measurement. Actually, the effect from the poor resolution will be shown at the beam test section.

The absolute gain value was investigated as a function of the voltage which is applied to anode wire. The ADC spectra around the 5.9 keV peak are fitted to Gaussian. The absolute gain was obtained using the following relation;

$$Gain = \frac{Q_{\text{induced charge}} \times \frac{C_{\text{anode-detector}}}{C_{\text{cathode-anode}}}}{5.9\text{keV}/W} \tag{4.2}$$

where, W stands for the average energy to generate a electron-ion pair (54 eV in case of CF_4), $Q_{\text{induced charge}}$ is the measured charge value, and the $C_{\text{anode-detector}}$ and $C_{\text{cathode-anode}}$ is the each capacitance between anode wire and TPC, and between cathode pad and anode wire, respectively. In this system, $C_{\text{anode-detector}}$ is 0.1 pF and $C_{\text{cathode-anode}}$ is 0.08 pF, and it was assumed that about 80

Figure 4.3 shows the result of gain measurement. This TPC has over 10^4 gain in pure CF_4, when the voltage of anode wire is +3.3 kV. In order to make suitable amplification to detect the signal, CF_4 needs stronger electric field than P10 gas.

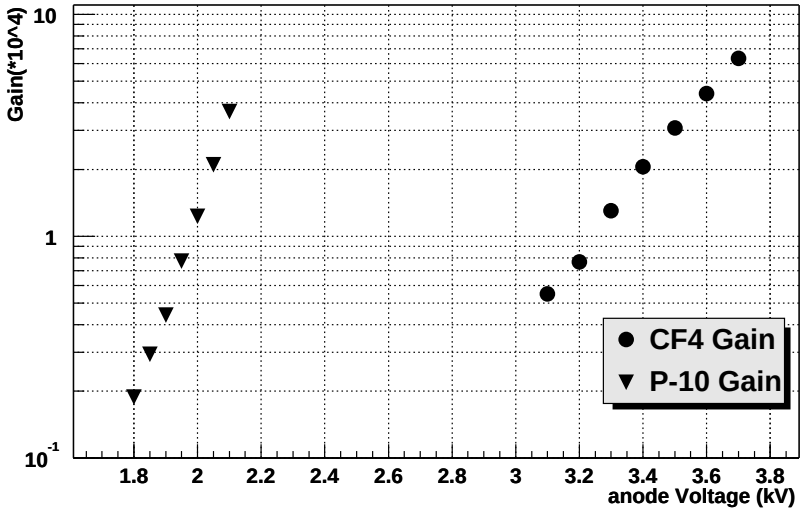

Figure 4.3: Gain of CF_4 and P10. This TPC has over 10^4 gain in pure CF_4, when the voltage of anode wire is +3.3 kV. In order to make suitable amplification to detect the signal, CF_4 needs stronger electric field than P10 gas.

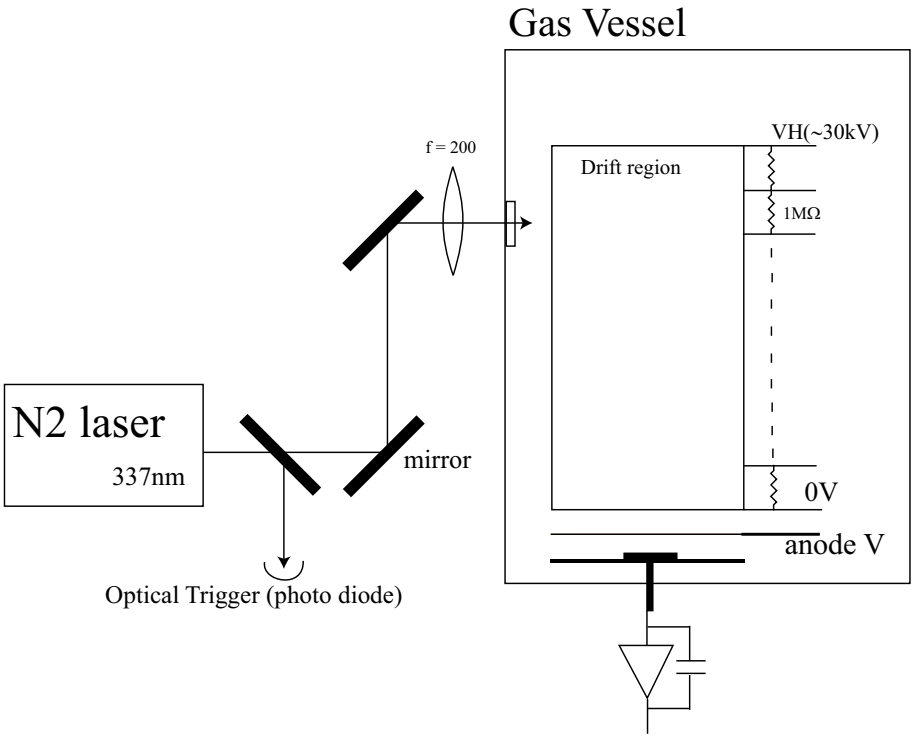

Figure 4.4: Sketch of the Setup of CF_4 gas test with nitrogen laser. A N_2 laser beam was reflected by two mirrors into a stationary drift cell through a quartz lens of 20 cm focal length. The focal point was in the middle of active drift volume. A portion of the laser beam is reflected to a photodiode which was used as a reference start counter for the timing measurements.

4.2 Drift velocity & diffusion

4.2.1 Setup

The drift velocity of CF_4 and P10 was measured by using the N_2 laser. Measurements were made using the experimental setup shown in Fig. 4.4. A N_2 laser beam was reflected by two mirrors into a stationary drift cell through a quartz lens of 20 cm focal length. The TPC gas vessel has six quartz windows for the laser beams with 15.8 cm distance between the two windows. The focal point was in the middle of active drift volume. To deal with single electron for this measurement, the probability of having an event per laser shot was set to be less than 10 % by attenuating the laser beam. A portion of the laser beam is reflected to a photodiode, HAMAMATSU Co. Ltd. S1722-03 (Si pin photodiode), which was used as a reference start counter for the timing measurements.

The flash ADC which was described in development section was used to record the signals. A t_0, start time of signal, is decided with the following equation;

$$t_0 = \frac{ADC_{pedestal} - b}{a} \tag{4.3}$$

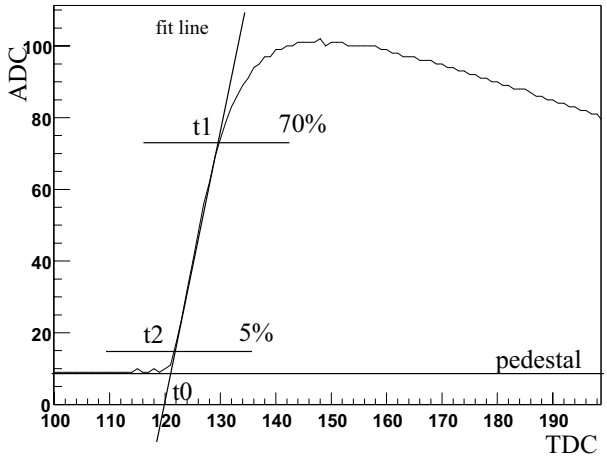

Figure 4.5: Typical shape of laser signal. Horizontal axis is TDC value and unit is 10 nsec. Vertical axis is ADC value with dynamic range of 8 bit (0 $\sim$ -1 V). About 10 samplings from t2 to t1 are used to obtain t0 for each signals. t0 is obtained using relation 4.3.

where, a and b are gradient and intercept of the fitted line shown in Fig. 4.5, $ADC_{pedestal}$ is pedestal value of ADC. a and b are obtained using following relation (minimizing χ^2 method):

$$a = \frac{\sum_{TDC=t2}^{n_{sample}} TDC_i^2 \sum_{TDC=t2}^{n_{sample}} ADC_i - \sum_{TDC=t2}^{n_{sample}} TDC_i \sum_{TDC=t2}^{n_{sample}} TDC_i \cdot ADC_i}{n_{sample} \sum_{TDC=t2}^{n_{sample}} TDC_i^2 - (\sum_{TDC=t2}^{n_{sample}} TDC_i)^2} \tag{4.4}$$

$$b = \frac{n_{sample} \sum_{TDC=t2}^{n_{sample}} TDC_i \cdot ADC_i - \sum_{TDC=t2}^{n_{sample}} TDC_i \sum_{TDC=t2}^{n_{sample}} ADC_i}{n_{sample} \sum_{TDC=t2}^{n_{sample}} TDC_i^2 - \Big(\sum_{TDC=t2}^{n_{sample}} TDC_i\Big)^2} \tag{4.5}$$

where, each ADC_i and TDC_i stand for recorded voltage and timing, respectively, and n_{sample} is number of samples from $TDC = t2$ to $TDC = t1$. $t1$ and $t2$ are the timing values when these ADC values are 70 % and 5 % of the pulse height respectively. With this method, time slewing due to pulse height difference can be corrected as shown in Fig. 4.5 The drift velocity is calculated using the mean value of $t0$ distribution, the longitudinal diffusion using the σ value of the distribution.

The water and oxygen was contained about 100 ppm and 30 ppm respectively in this measurement.

4.2.2 Test Result

The drift velocity was obtained using the following relation,

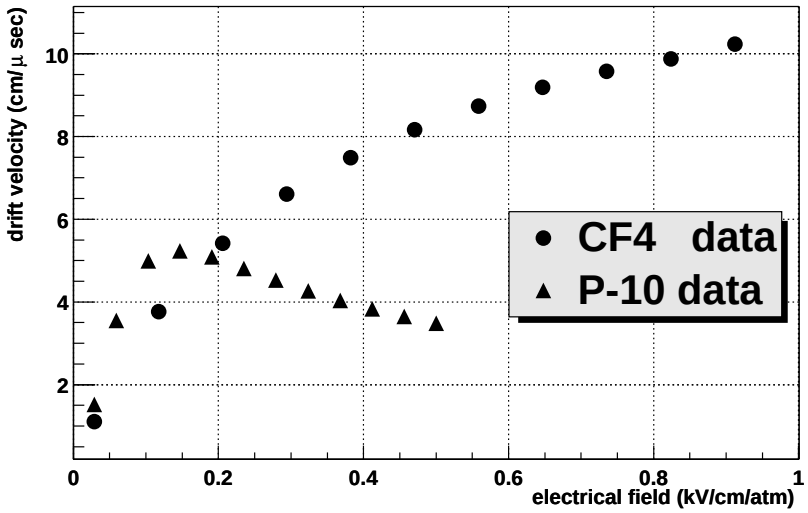

Figure 4.6: Drift velocity of CF_4 and P10. The drift velocity of CF_4 gas is more than 10 cm/μsec, when the electric field is 900 V/cm. The drift velocity of P10 at E $>$ 500 V/cm/atm could not be measured because of the discharge.

$$v_{drift} = \frac{z_1 - z_2}{t_1 - t_2} \tag{4.6}$$

where z_1 & z_2 are distances from the readout pads to the positions where the laser beam were injected, and t_1 & t_2 are arrival times of drift electrons.

The drift velocity of CF_4 and P10 were measured. As shown in Fig 4.6, the drift velocity of CF_4 gas is more than 10 cm/μsec, when the electric field is 900 V/cm.

From the fluctuation of the arrival time of single electrons which were realized with reduced laser intensity, longitudinal diffusion of CF_4 and P10 was obtained as shown in Fig. 4.7. The result of P10 gas measurement is consistent with the result of the simulation data. CF_4 has much smaller diffusion, less than 100 μm for 1 cm drift. The longitudinal diffusion of CF_4 gas is about 60 μm for 1 cm drift, when the electric field is 900 V/cm. It is consistent with the result of simulation data. When the electric field is less than 500 V/cm/atm, there is $\sim$10μm difference between the simulation results and the measurement data.

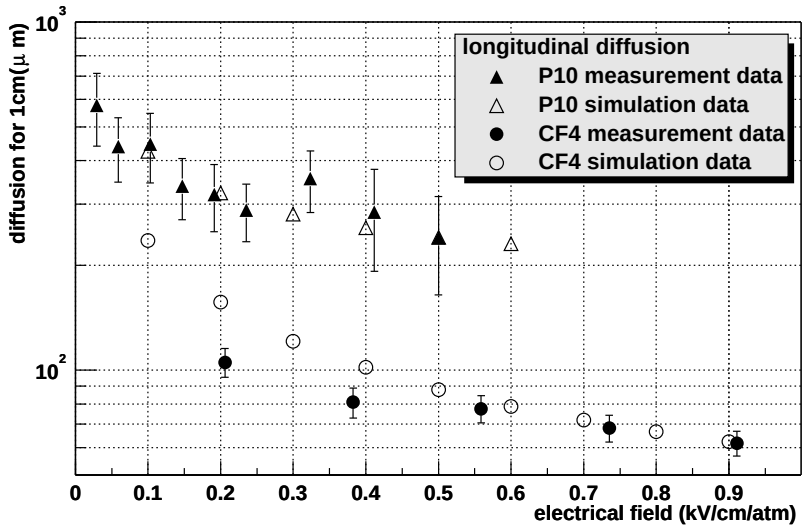

Figure 4.7: longitudinal diffusion of CF_4 and P10. CF_4 has much smaller diffusion, less than 100 μm for 1 cm drift. When the electric field is less than 500 V/cm/atm, there is $\sim$10μm difference between the simulation results and the measurement data.

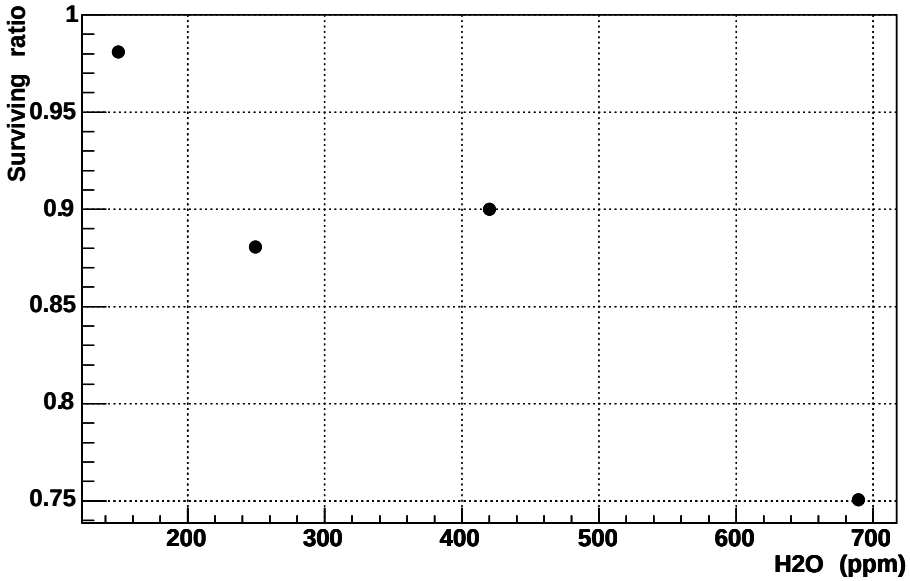

Figure 4.8: Electron surviving ratio after 15.8 cm drift (E = 900 V/cm) as a function of the quantity of water in the gas vessel. Each plot indicates the ratio of surviving electrons, $n_{after\ drift}/n_{before\ drift}$, after 15.8 cm drift. The attenuation is smaller, when the H_2O content is smaller.

4.3 Attenuation

Since addition of even small quantities of electro-negative pollutants to the chamber gas makes electron capture, it is important to study the drift property due to electron capture. Oxygen and water were used as the presence of electro-negative pollutants.

4.3.1 Setup

Attenuation length was obtained for CF_4 by measuring the collected charge at two different laser points. The setup is almost same as the setup of the drift velocity measurement. The quantities of water were monitored with moisture monitor as shown in Fig. 3.5.

4.3.2 Test Result

Fig. 4.8 shows the result of attenuation measurement of CF_4 as a function of the quantity of water in the gas vessel. Each plot indicates the ratio of surviving electrons, $n_{after\ drift}/n_{before\ drift}$, after 15.8 cm drift. The ratio was obtained using ADC value. The attenuation is smaller, when the H_2O content is smaller.

The maximum drift length of the proposed PHENIX TPC is expected to be 35 cm as shown in Fig 1.5. From the extrapolation of this measurement, the water content should be less than 150 ppm to keep the up to 90 % electrons in the PHENIX TPC with pure CF_4.

Chapter 5

Beam Test : Results and Discussions

5.1 Overview

The beam test was carried out using the secondary particles from internal target at T1 beam line of the Proton Synchrotron (PS) in High Energy Accelerator Research Organization (KEK). The characteristics of T1 beam line is listed in Table 5.1.

Characteristics of T1 beam	
Momentum range	0.3 - 2.0 GeV/c
Target size	1.0 mm diameter 15 mm long
Target material	Be,Al,Cu and W
Momentum bite	$\pm$ 1.0 %
Characteristics of focusing point	
Beam length	30 m
Horizontal magnification	2.63
Dispersion	-0.20 cm/% δp/p
Vertical magnification	4.65
Yield/$10^1$1 circulating protons at 1.5 GeV/c polarity - beam	0.7×10^{4}

Table 5.1: Parameters of T1 beam line

The main subjects for testing the prototype TPC are listed below.

- Position resolution
  Position resolution of the TPC with CF_4 gas was evaluated.

- Double track separation capability
  Capability to track multi trajectories separately in high particle density condition is required for this TPC.

- Particle identification
  With energy loss measurement, the particle identification capability was investigated.

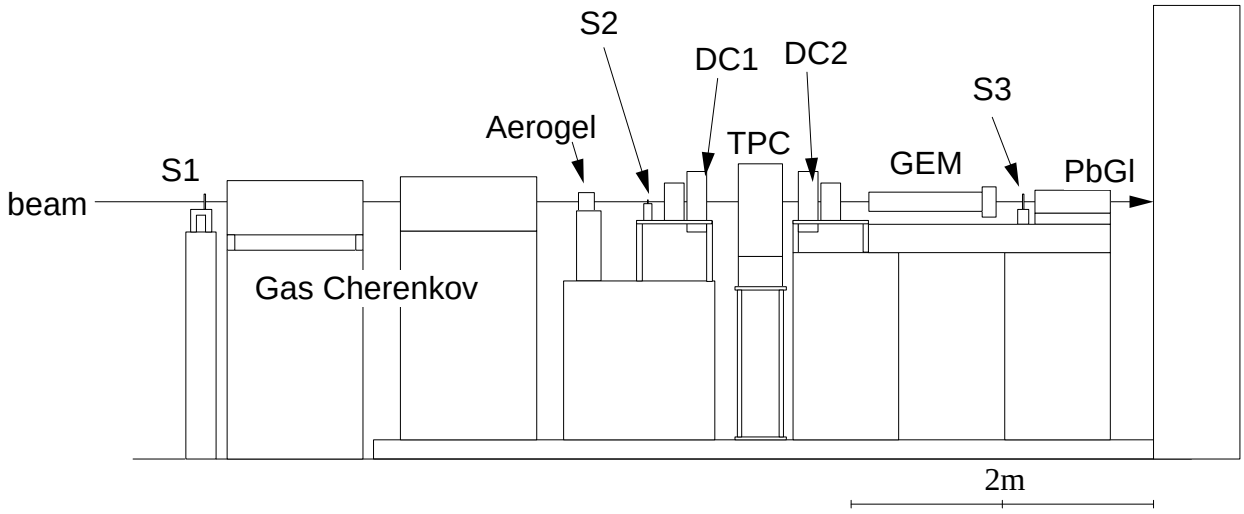

Figure 5.1: A schematic view of the beam test setup. TPC, GEM detector, Aerogel detector (ACC), three plastic scintillator (S1, S2 and S3), drift chamber (DC1 and DC2), lead glass calorimeter (PbGl), and gas Cherenkov detector (GCC) were used at the beam test. Two scintillators, GCC and PbGl were used for particle identification. DCs were used as reference tracker.

5.2 Setup

Fig. 5.1 shows a schematic view of detector setup. TPC, GEM detector, Aerogel detector (ACC), three plastic scintillator (S1, S2 and S3), drift chamber (DC1 and DC2), lead glass calorimeter (PbGl), and gas Cherenkov detector (GCC) were installed.

Two scintillators, GCC and PbGl were used for particle identification. DCs were used as reference tracker.

5.2.1 Scintillator

Light intensity	64 %
Maximum light length	391 nm
Decay time	1.5 nsec
Decay length	110 cm
reflection coefficient	1.58
H/C ratio	1.100
Density	1.032 g/cm^3

Table 5.2: Characteristics of scintillator (BICRON BC-420)

Three scintillators (BICRON BC-420) were used for trigger, time of flight and defining. Table 5.2 lists the characteristics of the scintillator. From coincidence of the signals from the

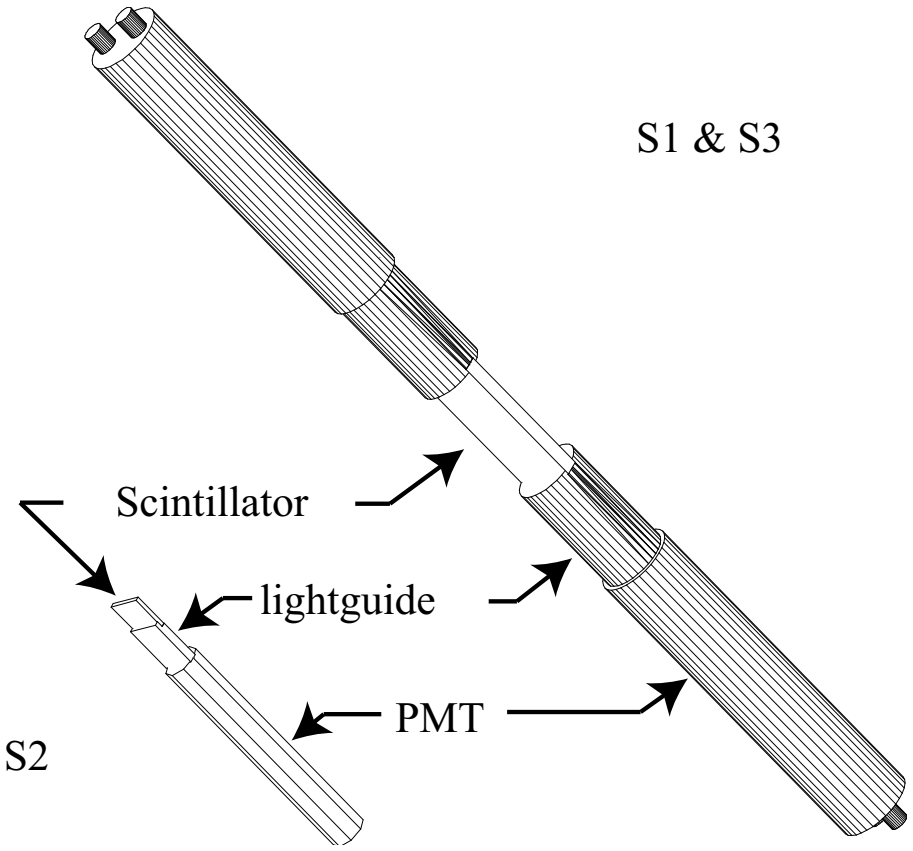

Figure 5.2: Layout of Scintillator. Each of S1 and S3 has two PMT and two 8.5 cm lightguides. S2 has a PMT and a 4 cm lightguide.

scintillators, acceptance of incident charged particle is defined, and an event trigger for readout is generated. Dimension of the scintillators are;

S1 : 100 mm (w) × 45 mm (h) × 10 mm (l)
S2 : 25 mm (w) × 25 mm (h) × 3 mm (l)
S3 : 50 mm (w) × 45 mm (h) × 10 mm (l)

Especially the geometry of S2 is 25 mm square, and the acceptance was mainly defined by S2. About 500 charged particles were accepted per spill with this setup. Each of S1 and S3 has two PMT and two lightguides (8.5 cm length) to readout the signals as shown in Fig. 5.2. The signals from S2 was readout by a PMT and a lightguide (4 cm length). Table 5.3 lists the characteristics of photomultipliers used for the scintillators.

And scintillator was used as Time Of Flight (TOF) for particle identification, mainly pion and proton separation. The flight length between S1 and S3 was 5909.5 mm. The ability of TOF will be described at Data Analysis session.

5.2.2 Gas Cherenkov Detector

In order to detect electrons, two gas Cherenkov detectors (GCC) were installed. Nitrogen gas was used as Cherenkov radiator, and pressure was about 4 atm.

Signals from these detector were used for generating trigger, when the data was taken for the purpose of studying double track separation capability. This will be described in the trigger section.

5.2.3 PbGl Calorimeter

Together with the gas Cherenkov detectors, Lead Glass calorimeter (PbGl) was used for electron identification. PbGl was mounted at the most down stream of the detector setup. The characteristics of PMT is listed in Table 5.3

	Scintillator		Gas Cherenkov	Lead Glass
	S1, S3	S2		
PMT Type	H1949	H6612	H6528	R1652-03 ASSY
PMT Diameter (inch)	2	3/4	5	3
Gain Typical	2.0×10^7	1.7×10^6	1.4×10^7	2.5×10^5
raise time (nsec)	1.3	1.3	2.5	4.3
transfer time (nsec)	28	14	54	18
Operation Voltage (V)	-2360 $\sim$ -2500	-1640	-2800	-1460

Table 5.3: Parameters of PMT

5.2.4 Drift Chamber

Two sets of drift chambers (DC1 and DC2) were used as reference tracking detectors to evaluate performance of position resolution capability of TPC. Fig. 5.3 shows the schematic view of wires of a drift chamber. A sensitive cell is 12mm square, and each DC consists of four layers. The cells in adjacent layers are staggered by half cell to each other.

DC acceptance was wide enough to cover the region defined by S2 as shown in Fig. 5.3. Two drift chambers (DC1), one for x-axis and the other for y-axis, were placed at upstream of TPC, and the other two drift chambers (DC2) were placed at downstream of TPC as shown in Fig. 5.1.

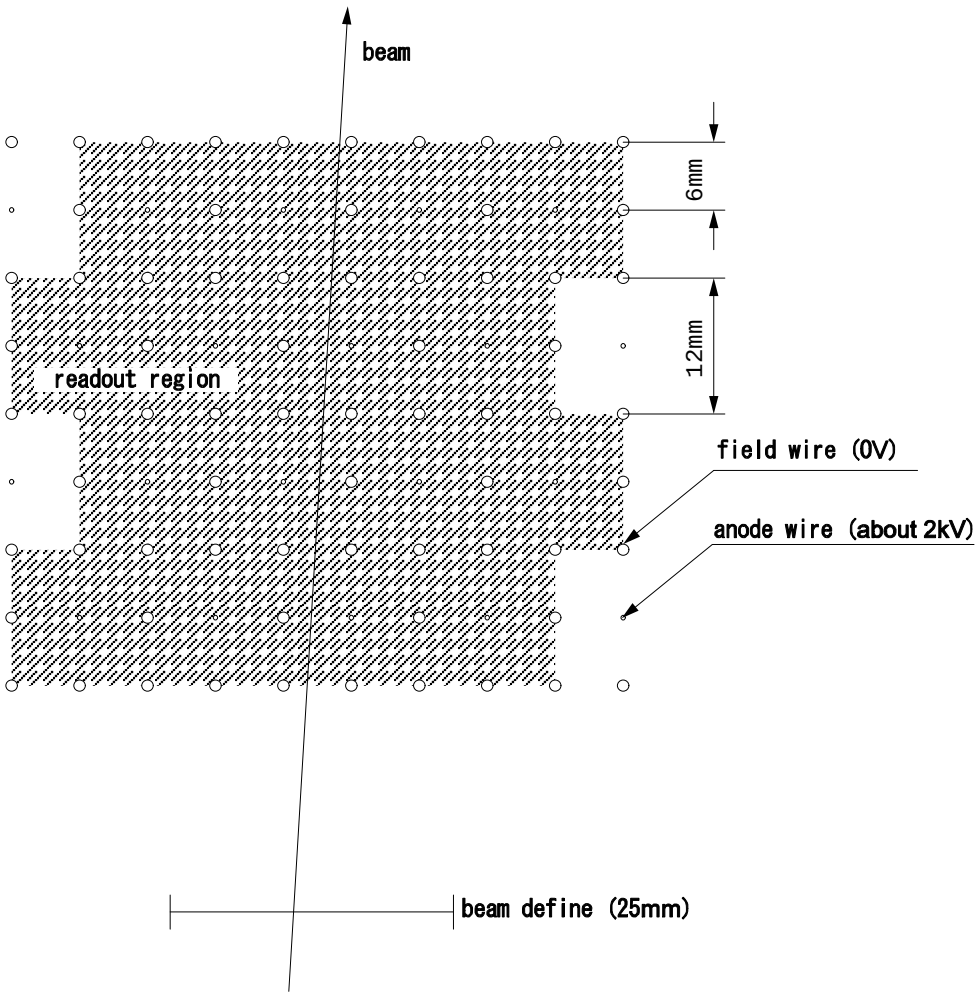

Figure 5.3: Layout of DC layers for each DC. Each DC has four layers for tracking. DC acceptance was wide enough to cover the region defined by S2.

5.2.5 Frontend Electronics & Trigger

VME system was used in this beam test. The used electronics modules are listed in Table 5.4.

ADC	CAEN V792AC	12bit resolution 400pC full scale 5.7μs/32ch conversion time 32 event buffer memory
TDC	CAEN V775AC	12bit resolution 136ns $\sim$ 1096ns full scale 5.7μs/32ch conversion time 32 event buffer memory
Flash ADC	Repic RPV160	100MHz conversion rate 8bit dynamic range (0V $\sim$ -1V) 8K words/ch data memory 150MHz bandwidth ADC
Trigger	GSI Trigger module	4 trigger ch ability of event synchronization rejection and event counter

Table 5.4: Details of Frontend Electronics modules

Two types of triggers were prepared for this beam test. One is a normal trigger which is the coincidence of three scintillators (S1, S2 and S3). This trigger was used for position resolution and particle identification test.

Another is a special trigger for evaluation of double track separation capability of TPC. Particle conversion at lead plate converter is occurred only when incident particle was electron. In order to select electron events for multi-track event from a converter, this trigger include the coincidence of signals from gas Cherenkov detectors. We could detect about 5 electrons a spill with p = 1 GeV/c.

5.2.6 DAQ System

In order to acquire data from VME modules described above, data was read from VME bus using on board CPU module (CES Co., RIO3). RIO3 sustains 100 MByte/s bandwidth on VME bus with a 400 MByte/s global memory bandwidth shared between different buses. And with direct memory access mode more than 20 MByte/s data transfer is possible from VME module to RIO3 memory.

New DAQ system was developed with Linux operating system. It is made up of two machines; RIO3 module and storage machine. Details of the DAQ system will be described in the appendix.

DAQ rate of about 200 events/spill, 1.6 MByte/spill, was achieved in this beam test.

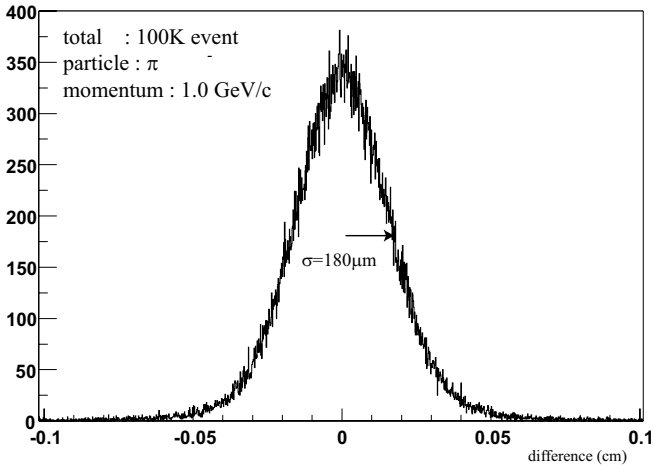

Figure 5.4: DCs position projection error of DCs track at TPC center (simulation). This error is assumed to be originated from multiple scattering between the sets of DCs.

5.3 Simulation Study for Beam Test

In order to plan the test setup, some parameters were defined by using GEANT3 simulator [27]. GEANT3 is a detector description and simulation tool with calculating the passage, interaction and energy loss of tracking particles through materials. GEANT3 can also show the graphical representation of the experimental setup and of the particle trajectories. Followings are topics calculated using GEANT3.

- multiple scattering of incident particles

  When the position resolution of TPC is evaluated, DCs were planned to be used as reference tracking detectors. Because of some materials between TPC and DC, mainly aluminum and G10, error from multiple scattering should be estimated. As a result of GEANT3 simulation, the evaluation of the position resolution with DCs is expected to consist of about 180μm as show in Fig. 5.4. This error is expected to be originated from multiple scattering between the sets of DCs. The resolution of DCs are assumed to be zero in this evaluation. In the analysis of real data, we did not use DCs information to measure position resolution of TPC.

- Lead converter thickness

  When the double track separation capability is investigated, a lead plate is placed behind S2 scintillator, in order to generate the multi-tracks to TPC for electron beams.

  The distance to the position of the lead plate and the thickness of that was fixed using the results from GEANT3 simulation.

  Fig. 5.5 shows number of electrons which are generated by a lead converter with the thickness of one radiation length (left figure) and two radiation length (right figure), respectively. The thickness was fixed to be one radiation length from this result. The

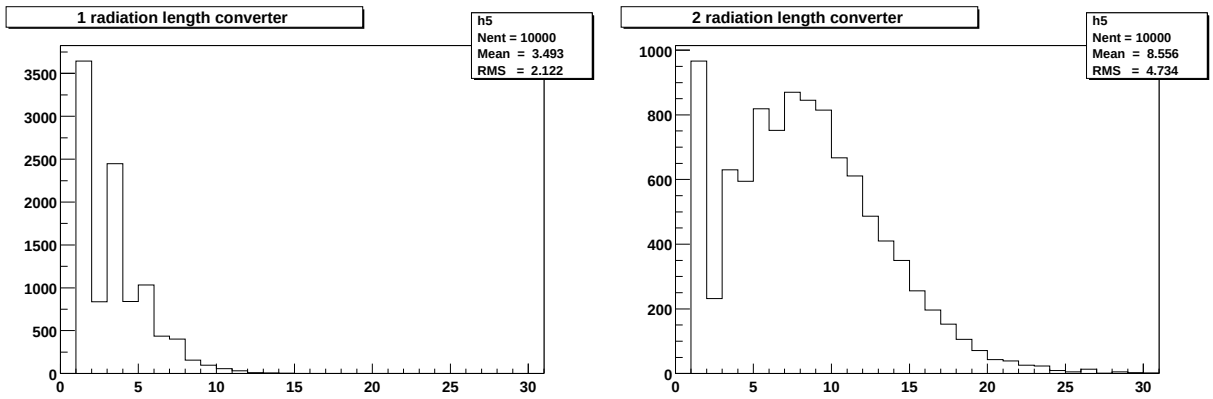

Figure 5.5: Number of electrons generated from Pb converter. Incident particle is electron with 1 GeV/c.

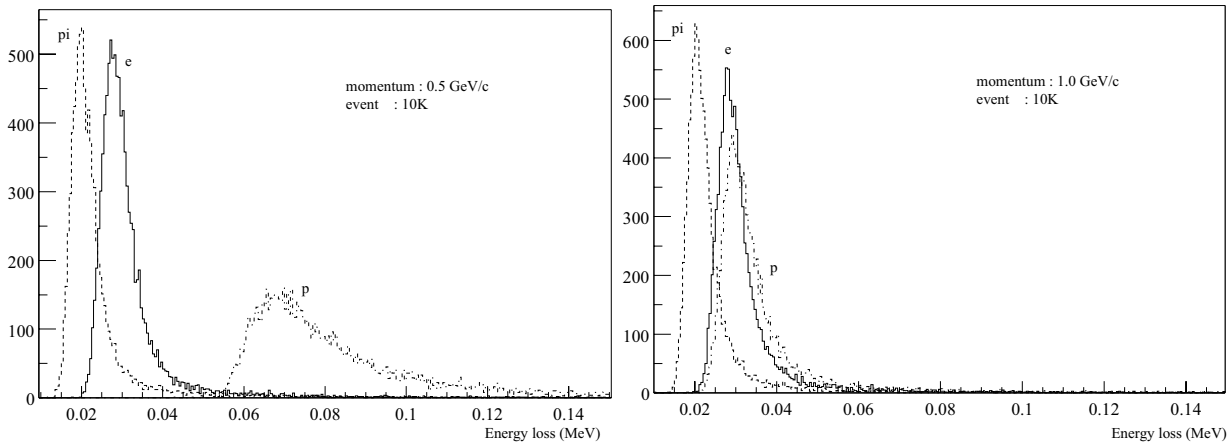

Figure 5.6: net energy loss from incident particles (simulated by GEANT3) for electron, pion, and proton. The track length is 17 cm.

distance between TPC and lead converter was fixed to 700 mm. This parameter was chosen go as to make incident double tracks to TPC uniform.

- Particle identification capability

  In order to measure energy loss per unit distance, dE/dX, the peak value from preamplifier is measured by the flash ADC. Electrons which are generated by ionization process are clustering according to a cluster size distribution [21]. The measured energy loss distribution changes in terms of the length measuring the clustered electrons.

  The energy loss is simulated by GEANT3 for each momentum and particle species, electron, pion, muon and proton. Fig. 5.6 contains net energy loss distribution about electron, pion and proton with 0.5 GeV/c and 1.0 GeV/c when the track length is 17 cm. Proton with 0.5 GeV/c separated clearly from other particles. The mean energy loss is close consistent with the value obtained from Bethe-Bloch formula.

  In order to simulate the measured charge value from clustered electron, HEED program was used for clustering the generated electrons [28]. HEED is a program that computes

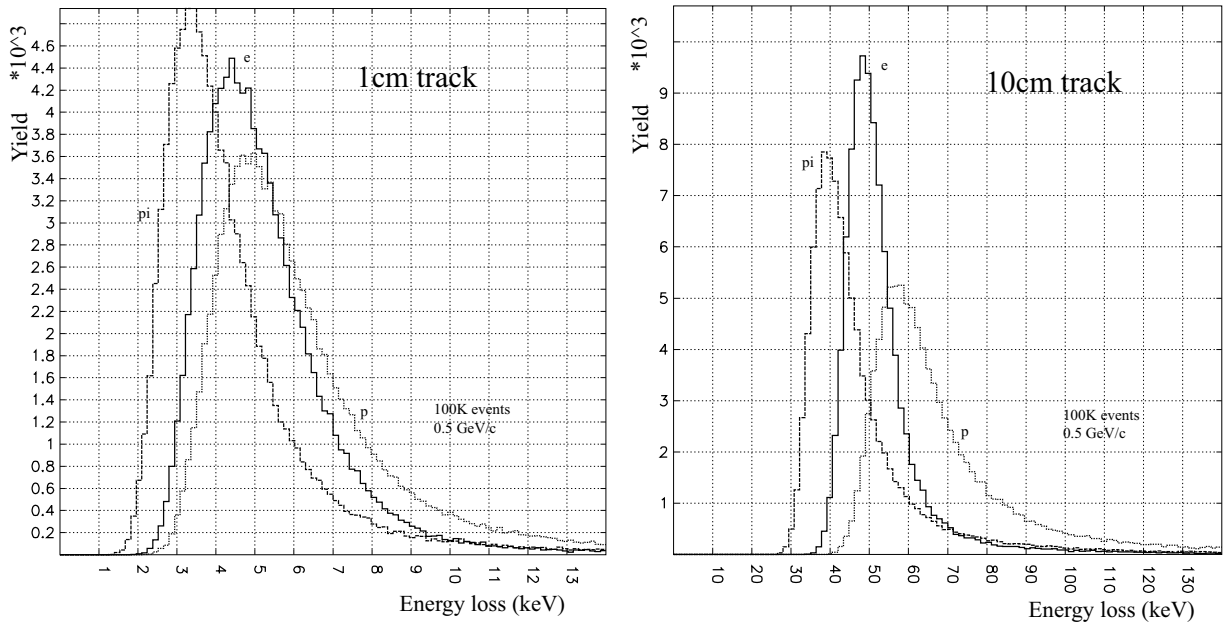

Figure 5.7: Detectable total energy of the electron clusters generated from particle energy loss (simulated by HEED).

in detail the energy loss of fast charged particles in gases, taking delta electrons and optionally multiple scattering of the incoming particle into account. Fig. 5.7 shows simulated measured energy loss about electron, pion and proton with different track length. 10 cm track is maximum in this simulator. Comparing with net energy loss distribution as shown in Fig. 5.6, proton with 0.5 GeV/c cannot separate clearly from other particles in this calculation.

In order to achieve good particle identification, the track length should be as long as possible. Track length for the evaluation of particle identification in this beam test was fixed to 5 cm, which was maximum.

5.4 Data Analysis

About 5 million events data were acquired.

5.4.1 Beam Profile

Trackings are reconstructed from DCs information with minimizing χ^2 method. Figure 5.8 shows the profiling of beam reconstructed from DCs information. Incident beam was mainly defined by S2 scintillator. Although incident beam was distributed nearly uniformly in the horizontal axis, the beam distribution in the vertical axis was biased upper.

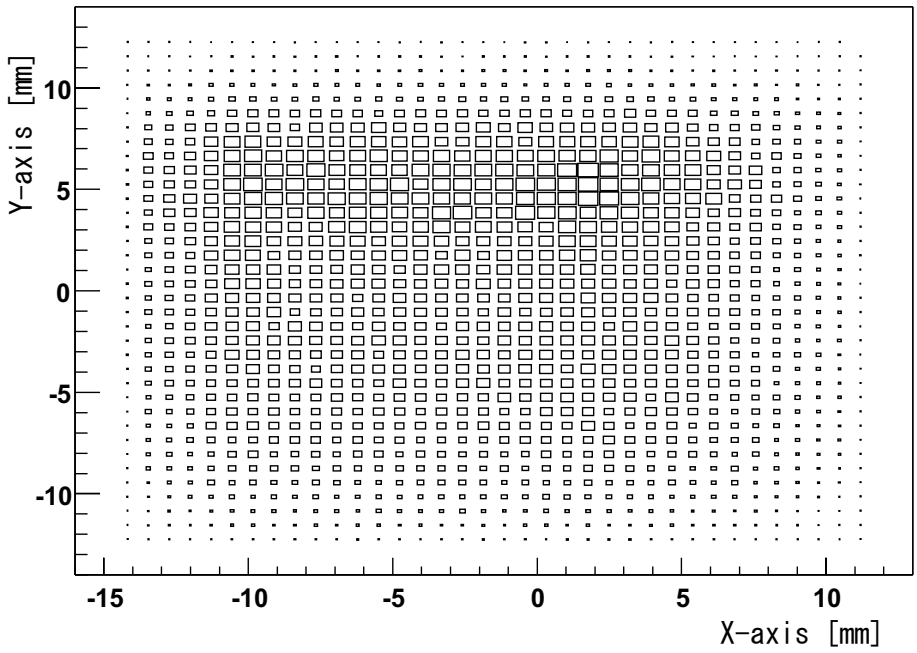

Figure 5.8: Beam Profiling at focusing point. This profiling was reconstructed from two sets of DCs information. Incident beam was mainly defined by S2 scintillator (25 mm square).

5.4.2 Particle Identification

Particle identification with Time of Flight, Gas Cherenkov and Lead Glass was used for evaluation of the TPC particle identification capability with energy loss measurement. Pions, protons and deuterons were identified with TOF measurement using S1 and S3. Electron was identified using GCC and PbGl.

Figure 5.9 shows the two type of correlation, one is the correlation between the ADC of GCC1 and the ADC of GCC2, the another is the correlation between the ADC of GCC1 and the ADC of PbGl. Each dashed lines indicates the criteria for electron identification. The contamination of the particle identification in this evaluation is assumed to be zero. Except for the case of the momentum with 0.5 GeV/c, electrons were not used for the following evaluation because of the low statistics.

Figure 5.10 shows TOF distribution for each momentum. Each shaded region in the figure indicates the region used for an identified particle in the evaluation of the capability of TPC particle identification. The contamination of the particle identification using TOF is assumed to be zero.

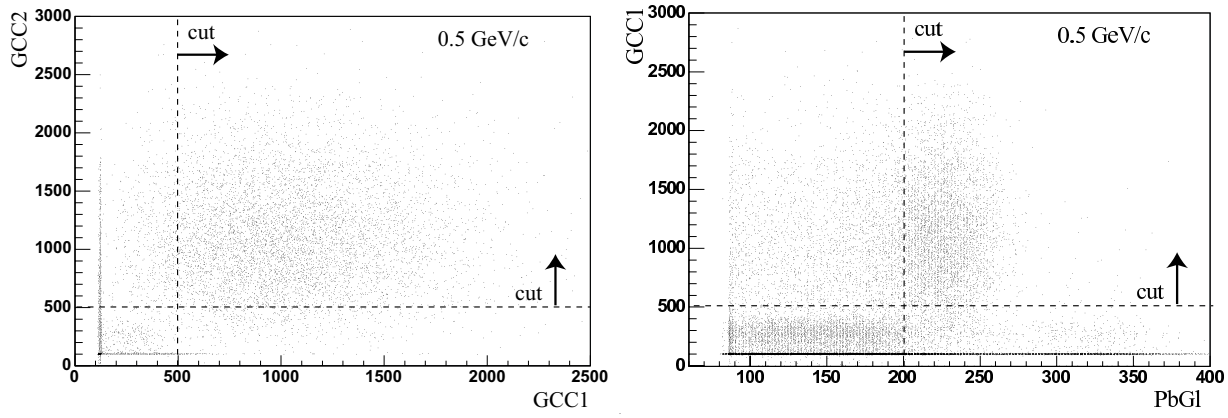

Figure 5.9: Correlation between ADC of GCC1 and ADC of GCC2 (right figure). Correlation between ADC of GCC1 and ADC of PbGl (left figure). Dashed lines indicate the criteria for electron identification. Electrons for evaluation of TPC particle identification capability is selected as shown in figure. identification.

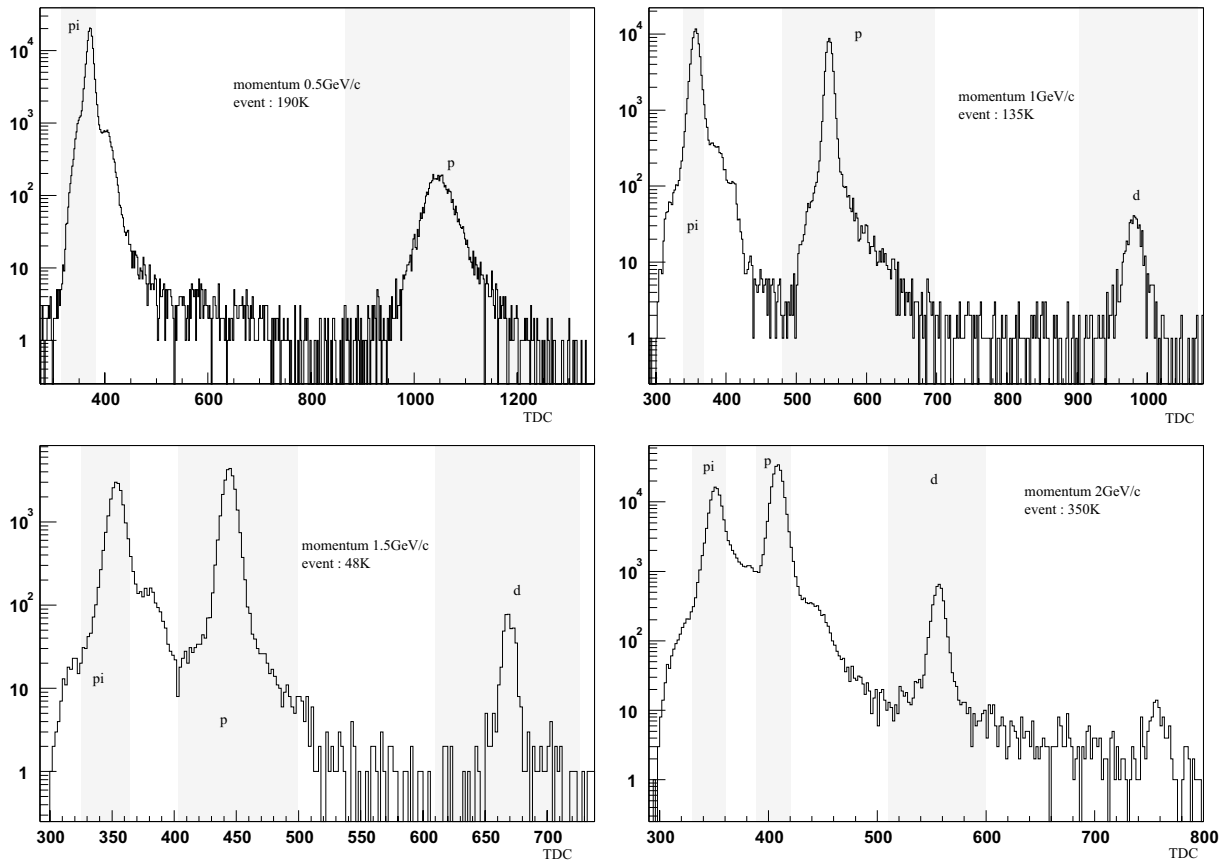

Figure 5.10: Distribution of TOF for each momentum. Each shaded region in the figure indicates the region used for an identified particle in the evaluation of the capability of TPC particle identification.

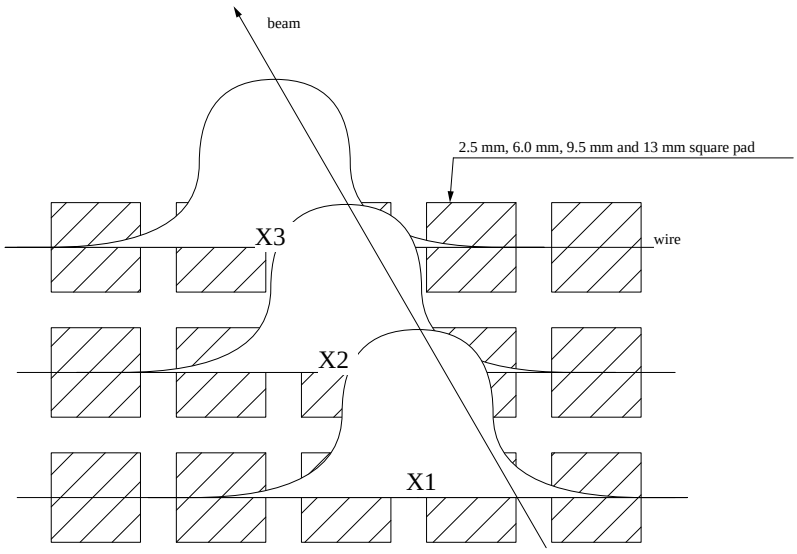

Figure 5.11: Sketch of signal readout from cathode pad. The position along the anode wire for each layer was obtained by charge ratio method. The direction of incident beam was nearly perpendicular to the anode wire.

5.5 Test Result

With data set for the evaluation of TPC, following topics were studied. The electric field of the drift region of TPC was set to 910 V/cm. The gas vessel of TPC contained water of about 50 ppm.

5.5.1 Position resolution

π^- beam with 1 GeV/c was used for this test. Three adjacent layers of TPC cathode pads were read in this beam test. The layers are positioned as shown in Fig. 5.11. Hereafter, the positions along the wire direction and in the drift direction are refered to as X and Y, respectively.

Position X was obtained using charge ratio method as following relation:

$$X = \frac{\sum x_i \cdot q_i}{Q} \tag{5.1}$$

where, each of x_i stands for the position of the center of each pad, q_i stands for the value of charge (ADC), and Q is value of total charge. When 2.5 mm square pads are used for readout, each signal was distribute over 5 pads.

Position Y was obtained from the product of timing information and drift velocity. When the electric field is 910 V/cm, drift velocity in pure CF_4 is 10.4 cm/μsec. T0 information was obtained as timing information using same method that described at gas test section.

The position of each layer is decided independently each other. Position resolution in the drift direction and along the wire direction were obtained from the r.m.s. value of the following function;

$$\Delta X = X_2 - \frac{X_1 + X_3}{2} \tag{5.2}$$

$$\Delta Y = Y_2 - \frac{Y_1 + Y_3}{2} \tag{5.3}$$

where X_i (Y_i) is a position obtained at each layer. It is assumed to be position resolution of each layers are same. with the From propagation of errors, the position resolution of the unit layer is obtained using following relation:

$$\Delta X = \sqrt{\frac{3}{2}}\delta x, \qquad \Delta Y = \sqrt{\frac{3}{2}}\delta y \tag{5.4}$$

where δx (δy) is the position resolution of unit layer.

Position resolution was measured for parameterized pad size (2.5 mm, 6.0 mm, 9.5 mm), incident angle (15, 30, and 45 degree) and incident height (5.4 cm, 19.4 cm and 33.4 cm distance from anode wire). Fig. 5.12 shows the results of the measured position resolution as a function of the drift length. The left figures show the resolution along the anode wire direction, and right figures show the resolution in the drift direction. The errors are defined by the static error for each measurement. A position resolution of 100 μm along the wire was achieved with 2.5 mm square pads. The resolution along the anode wire is worse as the incident angle is bigger, because induced charge distribute more broadly at larger incident angle. The resolution doesn't depend on the drift length strongly, because of the small diffusion of CF_4. The resolution in the drift direction is same for each type of pads. A position resolution of about 500 μm in the drift direction was achieved with each condition.

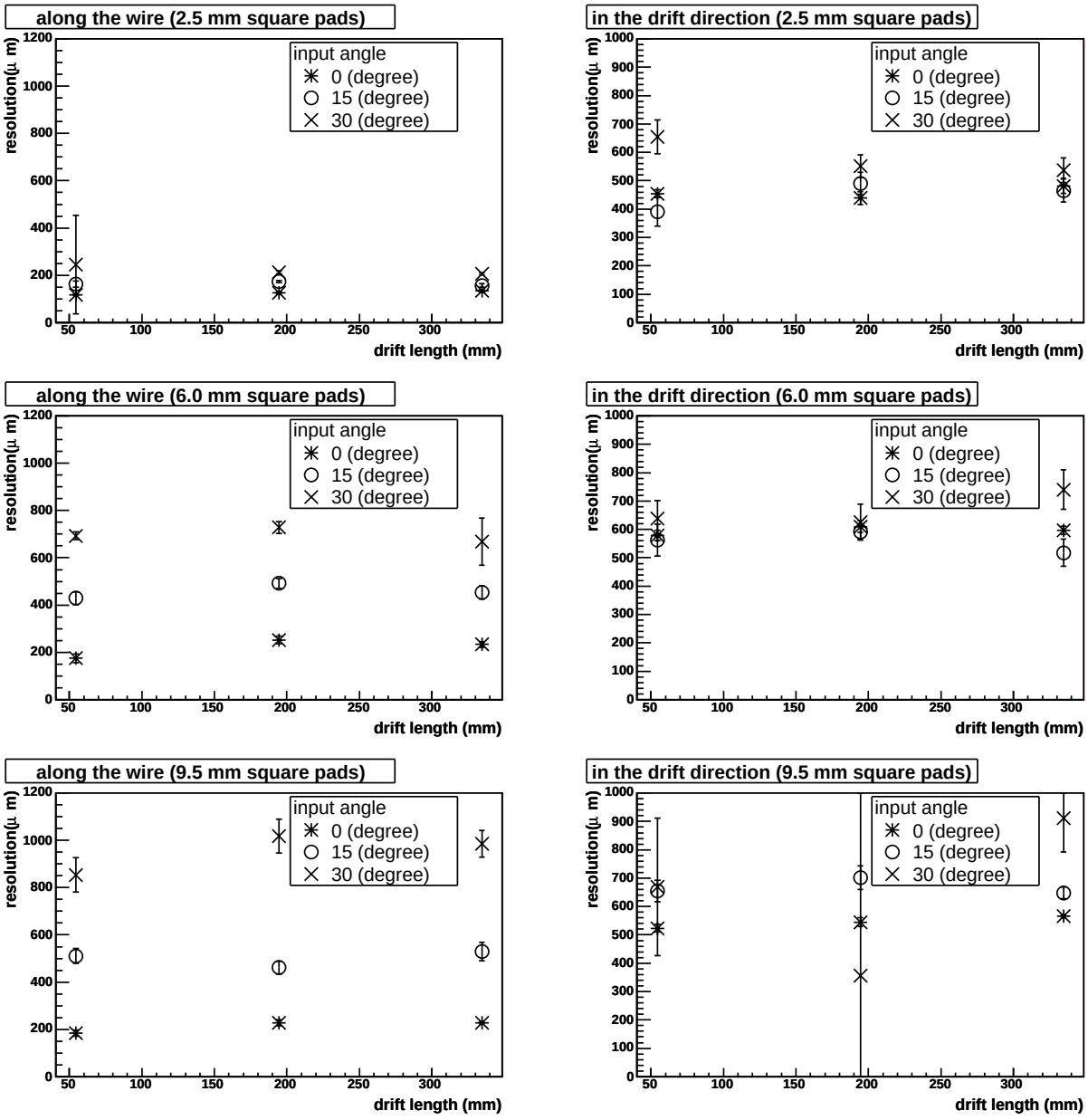

Figure 5.12: Position resolution as a function of the drift length. The left figures show the resolution along the anode wire direction, and right figures show the resolution in the drift direction. The errors are defined by the static error.

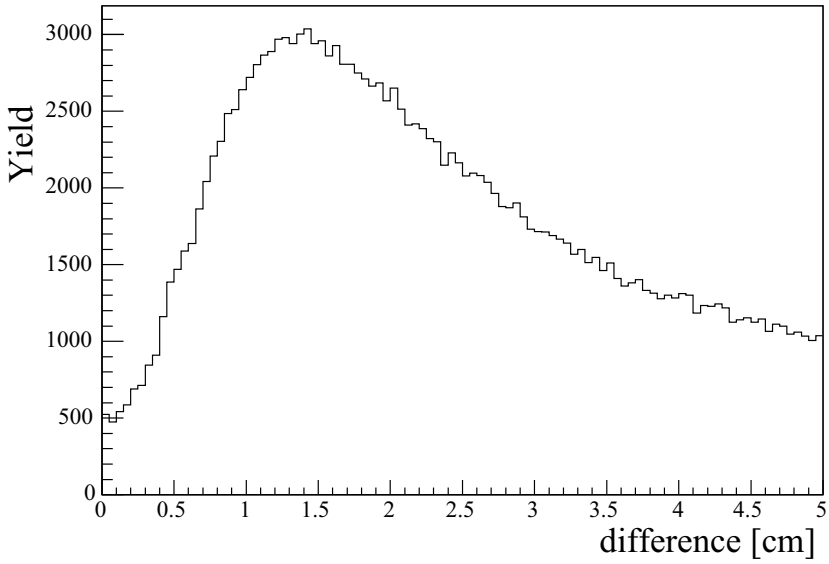

Figure 5.13: Difference in distance in the drift direction of identified double tracks obtained from GEANT simulation.

5.5.2 Double Track Separation

In this beam test, the capability of the double track separation in the drift direction with TPC was evaluated. In order to identify the two track events, the shape from TPC pre-amplifier was used. Fig. 5.15 shows the typical shape taken from flash ADC data.

If double tracks are incident to TPC, two rising edges appear as shown in the left figure of Fig. 5.15. Using a algorithm, a double track could be identified by recognizing the significant transition of the gradient, the capability of double track separation is evaluated. From the GEANT simulation, the distribution of double tracks is estimated and shown in Fig. 5.13. The detection efficiency was obtained form the ratio of number of tracks obtained from measurements with the algorithm over number of tracks obtained from GEANT3 simulation. Fig. 5.14 shows the result of double track separation. The horizontal axis is the difference in distance between the identified double tracks in *cm* and the vertical axis is the detection efficiency. For normalization, the saturation shown in the distribution is assumed to be the detection efficiency of 100 %. This TPC can detect a double track effectively when the distance in the drift direction between the double track is more than about 1.5 cm, when detection efficiency of more than 50 % is chosen.

This result mainly depends on the rising time of the signal shape. The typical rising time is 110 nsec, as shown in the right figure of Fig. 5.15. Since the drift velocity is about 10 cm/μsec in this condition, it is expected to be available to identify the double tracks when the difference in distance is longer than about 11 mm. The rise time is expected to depend on the slew rate of the frontend electronics system. As a next step, it is proposed to develop a new type of FEE which has large bandwidth and fast slew rate.

The rise time of the direct signal from cathode pad is expected to be about 30 nsec. The double track separation capability is limited by this rise time, and to be about 4 mm. In order

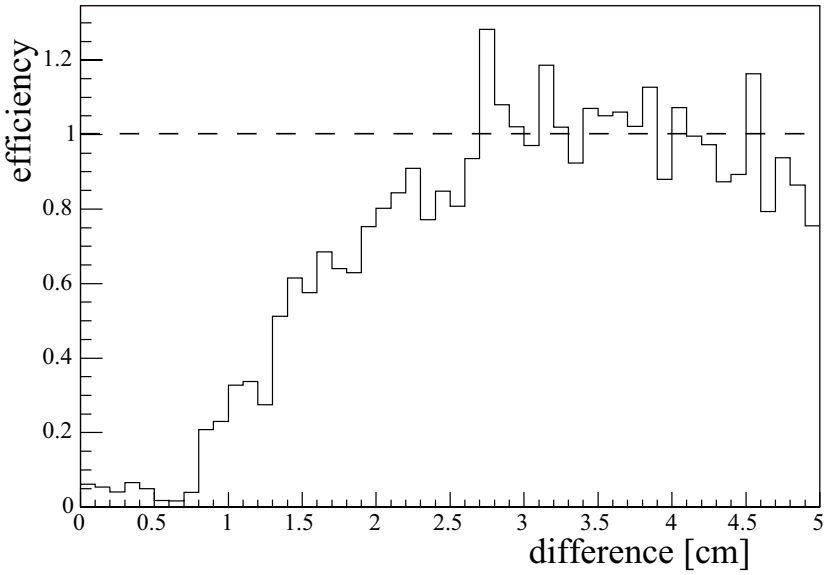

Figure 5.14: Difference in distance in the drift direction of identified double tracks. Horizontal axis is the ratio of identified double tracks in simulated double tracks. Figure 5.13 is used as reference distribution in this evaluation.

to make double track separation capability less than 1 mm, the rise time should be faster than 10 nsec. The rise time of the direct signal is defined largeness of electron cloud and depends on the readout geometry. Also, GEM may enable to make fast signals, because the ion tails are not shown from the anode pads and only electron signals are shown with GEM readout.

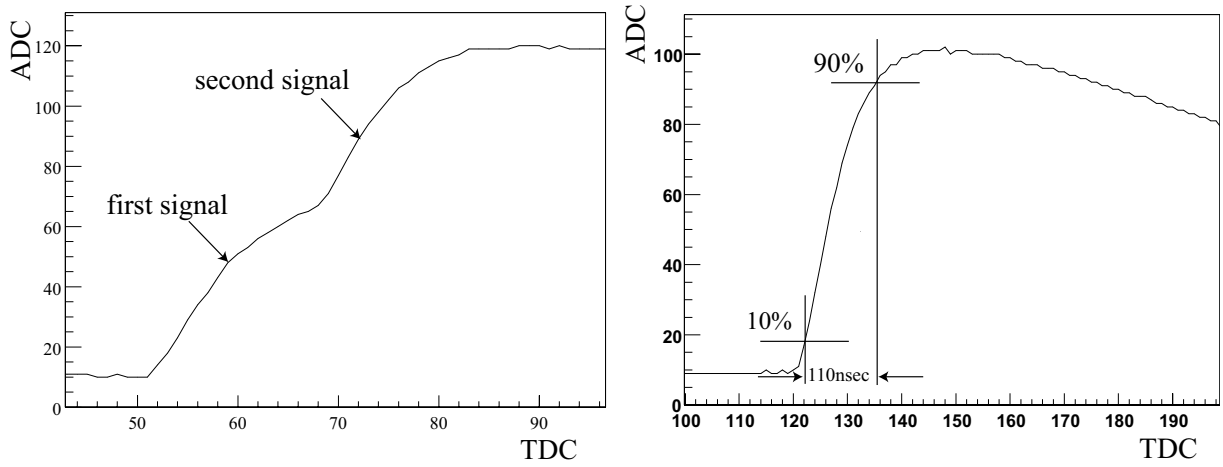

Figure 5.15: Typical shape of signal from FADC readout data for unit signal and double signal. The typical rising time is 110 nsec.

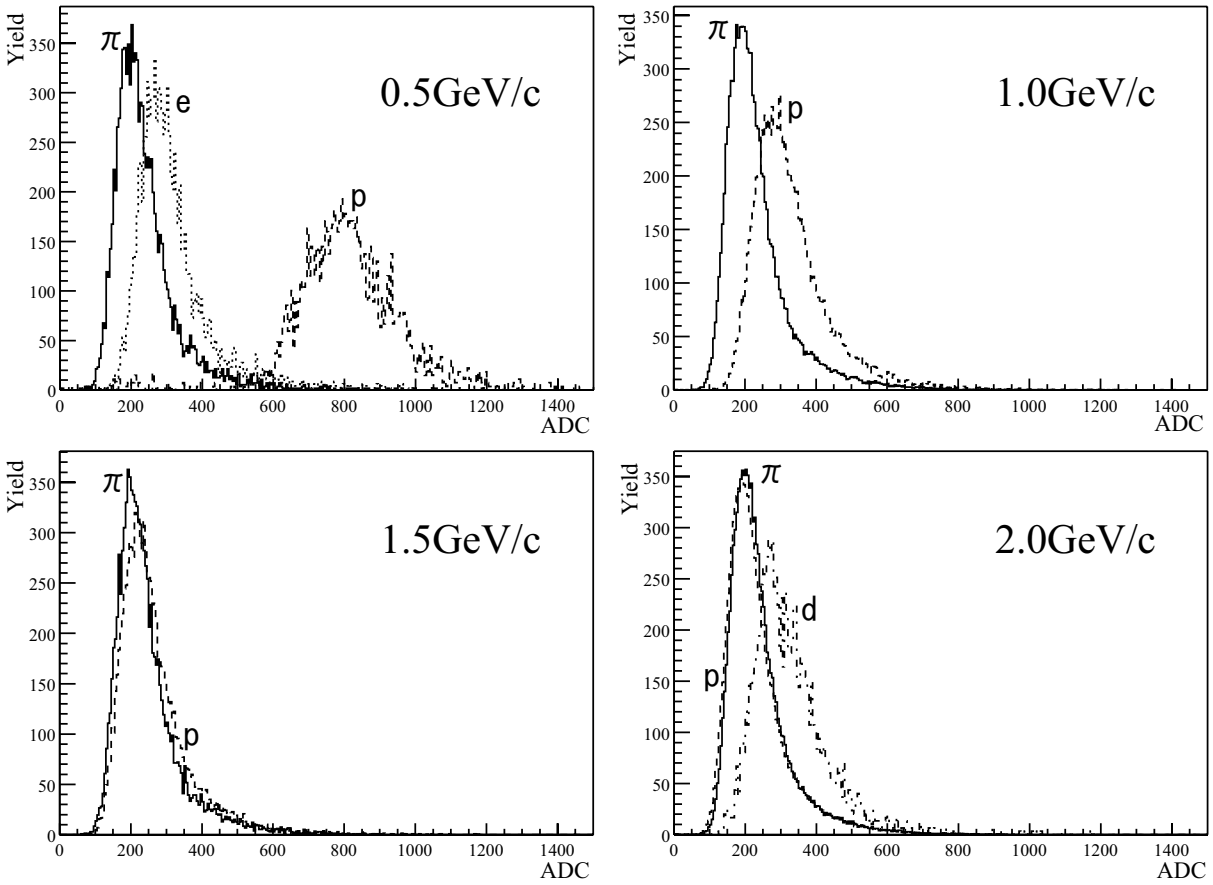

Figure 5.16: ADC sum distribution of each particle, electron, proton, and deuteron. Each figure shows the ADC distribution at each momentum.

5.5.3 Particle Identification capability

With the reference where incident particles are identified by GCC and TOF, the particle identification capability of TPC with CF_4 is evaluated. Fig. 5.16 shows the distribution of the sum of ADC value for each particle, 0.5 GeV/c, 1.0 GeV/c, 1.5 GeV/c, and 2.0 GeV/c. The distribution which has low statistics are not shown and not used for following evaluation. The length of the trajectory is 5 cm. Protons with 0.5 GeV/c are identified with rejection factor of 100 and efficiency of 95

From the result of ADC distribution for each particle, The values of dE/dX were evaluated from measurements for each particle assuming that energy loss depends only on velocity. Fig. 5.17 shows the expected ADC plots. Points indicate the mean value of the ADC and the errors indicate the r.m.s. value of the ADC distribution. Electron and pion dE/dX dependence of momentum and rejection factor of pion are evaluated from this result. When electron efficiency of 92 % is chosen, π meson can be rejected by factor of 11 in the momentum range of $p \leq$ 80 MeV/c using this type of TPC. When the particles minimum ionizes, the energy resolution is about 35 %.

The sum of the ADC value of above results were for 5 cm particle track length. In order to

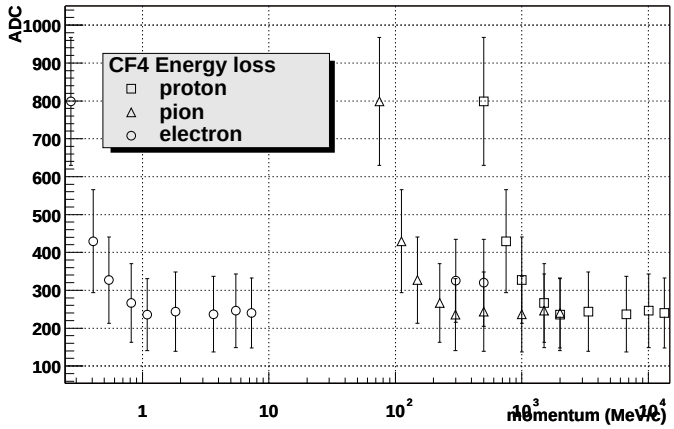

Figure 5.17: Expected ADC sum plots for each particle. The errors are defined by the r.m.s. of each distribution. Energy loss is assumed to depend only on velocity.

estimate the ADC value when the track length becomes longer, the expected distribution was simulated using inverse transform method, one of the Monte-Carlo techniques. The cumulative distribution function is given by Eq. 5.5, for each distribution of Fig. 5.16.

$$F(a) = \int_{-\infty}^{a} f(x)dx \tag{5.5}$$

And a unique x was chosen from the integrated probability which is itself a random variable which will occur with uniform probability density on $[0, 1]$.

Fig. 5.18 is the result using inverse transform method from the distribution in Fig. 5.16, where the track length is 1 m. Expected ADC value is decided at each β value, and plotted as shown in Fig. 5.19 as well as Fig. 5.17. Rejection factor of pion is evaluated with expected dE/dX dependence in Fig. 5.19 for 1 m track length. π meson can be rejected by factor of 11 in the momentum range of $p \leq 120$ MeV/c using this type of TPC, when electron efficiency of 92 % is chosen.

The energy resolution of the STAR TPC [29] is 7 % for a track that crosses pad-rows of 60 cm length. P10 is used as chamber gas in the STAR TPC. Using inverse transform method as above, the extrapolated energy resolution of the TPC with CF_4 for a track that crosses pad-rows of 60 cm length is expected to be about 12 %, which is much worse than that of STAR TPC. This is consistent with the result of gain measurement as shown in Fig. 4.2.

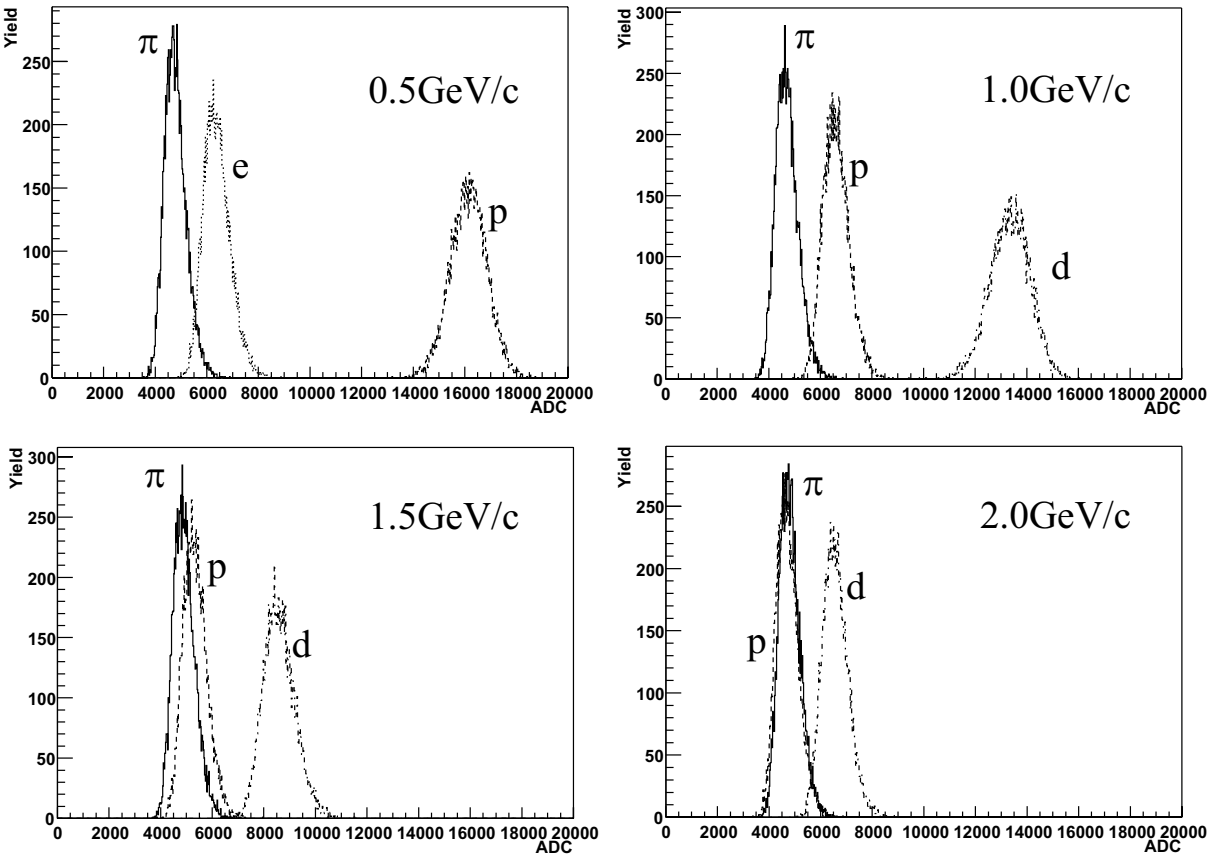

Figure 5.18: ADC sum distribution from simulation. These distributions were calculated with inverse transform method. Each figure shows the ADC distribution at each momentum.

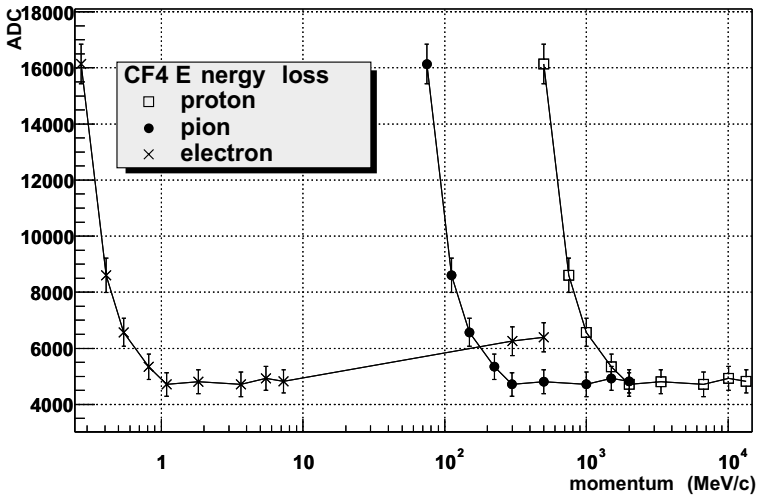

Figure 5.19: Expected ADC sum plots for each particle from simulation. The errors are defined by the r.m.s. of each distribution. Energy loss is assumed to depend only on velocity.

Chapter 6

Conclusion and Future Plan

A prototype TPC for experiments with heavy ion collisions was developed. This TPC was designed to use CF_4 gas as the chamber gas. The basic characteristics of CF_4, gas gain, drift velocity, longitudinal diffusion, and attenuation, were measured with the prototype TPC. This TPC has over 10^4 gain in pure CF_4, when the voltage of anode wire is +3.3 kV. In order to make suitable amplification to detect the signal, CF_4 needs higher HV of anode wire than P10 gas. When the electric field of more than 900 V/cm is applied, the drift velocity and longitudinal diffusion of CF_4 are about 10 cm/μsec and about 60 μm for 1.5 cm electron drift, respectively.

The performance of this prototype TPC with CF_4, position resolution, double track separation, and particle identification capability, were checked with beam test. Position resolution of 100 μm along the anode wire was achieved with 2.5 mm square pad. Position resolution of about 500 μm in the drift direction was achieved. Two tracks whose difference in distance are more than 1 cm in the drift direction can be identified as double tracks. This type of TPC allows that π meson can be rejected by factor of 11 in the momentum range of $p \leq 80$ MeV/c, when the electron efficiency of 92 % is chosen.

Double track separation capability is expected to be improved with the new type of frontend which has faster slew rate.

As a result from the gas tests, it is verified that the TPC with CF_4 gas has high performance, which is suitable for the operation under such particle multiplicity at PHENIX.

New type of TPC with GEM readout is planned to be developed in order to improve the capability of TPC. There are some improvements with GEM readout. The ions generated from the avalanche ionization will not reach the drift region because of the electric field made by GEM readout. This feature should help improved performance without the distortion of electrical field from the ions. And since this makes fast signal because of no ion tails, good double track separation of $\sim$500 μm is expected. The evaluation of the GEMTPC is planned as a next step.

Acknowledgment

It is a great pleasure to express my science gratitude to Prof. H. Hamagaki who has led me to this interesting and exciting field of science. I also appreciate him for his continuous encouragement and appropriate advice when needed. I would also like to pay my respect to Dr. K. Ozawa for his persevering guidance, discussion, and support throughout this work. Without their help, my work could have been reduced to being beside the mark.

I am much obliged to Dr. K. Oyama, Dr. T. Sakaguchi, and Mr. T. Matsumoto. They gave me a lot of useful information as a maker of the prototype TPC and the frontend electronics. I acknowledge Dr. M. Inuzuka for his training me in physics. He gave me kind lectures on fundamental physics.

Special thanks are due to all the collaborators of the T538 beam test, in particular to Dr. S. Sawada and Dr. S. Yokkaichi. Discussion on the beam test with these people has been so much helpful for me as their presence itself. I acknowledge Dr. M. Sekimoto for her support of this beam test. Without her support, I would not be able to succeed the beam test. I hope to acknowledge the KEK beam channel group and experimental support group, in particular to Dr. M. Ieiri. I acknowledge students and stuffs who belong to Tsukuba Univ. for their collaboration. I'd like to thank Mr. Y. Nagata who help me develop a new data acquisition system.

I'd like to give thanks to my fiancee, Miss A. Takizawa, for her encouragement. She gives me moral support in a lot of ways.

Finally, but not least, I express my thanks to all the members of Hamagaki group. I would particularly like to appreciate Mr. S. Kametani, Mr. F. Kajihara, Mr. S. Oda, and Mr. Y. Yamaguchi for their advice and support. I am also grateful to Mr. N. Kurihara and Mr. T. Gunji for their friendship and fruitful discussion as nice colleagues.

Appendix A

Development of DAQ

DAQ system for beam test was newly constructed. The driver and application code is written in C language and C++ language with NOVA program, buffer manager, and CERN ROOT program for online monitor. NOVA buffer manager program is used in UNIDAQ system. UNIDAQ [31] is online data acquisition system with multi process in a CPU. New DAQ system constitutes this buffer manager for online processings (recording, analyzing...). ROOT [30] library is mainly used for online monitor part of this new DAQ system. We can make histograms and graphs with this library. Using NOVA and ROOT program, this DAQ system was constructed for multipurpose analysis program.

This system consists of two computers connected by 100Base-T network interface. Each computer has the each role for DAQ system. And both computers are operated by Linux operating system.

A computer is a VME module, RIO3 by CES Co.. This module doesn't have hard disk drive, but Power PC CPU and 128 MByte memory. Sugar Hat Linux is used as operating system. RIO3 module is used for following roles:

- Data reading
  RIO3 reads data from VME modules (ADC, TDC and Flash ADC) via VME bus with the start of readout trigger from trigger module. It is allowed Direct Memory Access (DMA) data transfer and the data from attached VME bus to the memory on RIO3 board directory in this DAQ system. And the processor is freed from involvement with the data transfer, thus speeding up overall computer operation. This system with RIO3 enable to transfer data more than 20 MByte/s.

  In this time, the driver libraries for RPV-160 by REPIC Co. Ltd, V792 and V775 by CAEN Co., and trigger module by GSI were developed for DAQ operation.

- Storage data temporarily
  RIO3 has stored data taken as above in the high memory buffer that installed in RIO3 since the end of beam spill. The span of the spill is 2 sec, and next spill is coming after 2 sec, total 4 sec cycle in this beam test.

  The high memory buffer is a buffer located at the end of the system memory which is not under the control of the Linux virtual memory manager. It can be reserved by telling

Linux to use less memory than what is actually available. RIO3 board has 128 MByte of system memory and a high memory buffer of 64 MByte, half of available, is reserved and remained 64 MByte is used as Linux virtual memory.

- Data transfer
  RIO3 transfers data to host computer via TCP socket between beam spill. This transferring program is written using a NOVA library.

Another computer is a normal PC, called host computer. Red Hat Linux 7.2 is used as operating system. Host computer is used for following roles:

- Data buffering
  Using NOVA buffering manager, the data from RIO3 module is buffered each event. These buffered data is forwarded to storage and online monitors.

- Storage data in HDD
  All data buffered is recorded in hard disk drive.

- Online monitor
  A part of buffered event is analyzed by online monitor. This online monitor is written in C++ language with CERN ROOT library. It is easy to expand the versatility of online monitor system as the requirement of DAQ users.

Figure A.1 shows the simple schematics of DAQ system as above. There is one process in RIO3 and there are more than three process in host computer for DAQ operation. "Collector" is running in RIO3 in order to read data and put data to host computer. "novand" is running in host computer in order to receive the date from RIO3 and put the buffer reserved. "nova" is running in order to manage the buffer and forward the buffered data to the processes of online monitor and storage. "recorder" is running in order to record the all data sent from "nova" process. And some processes of online monitor are running to check the data.

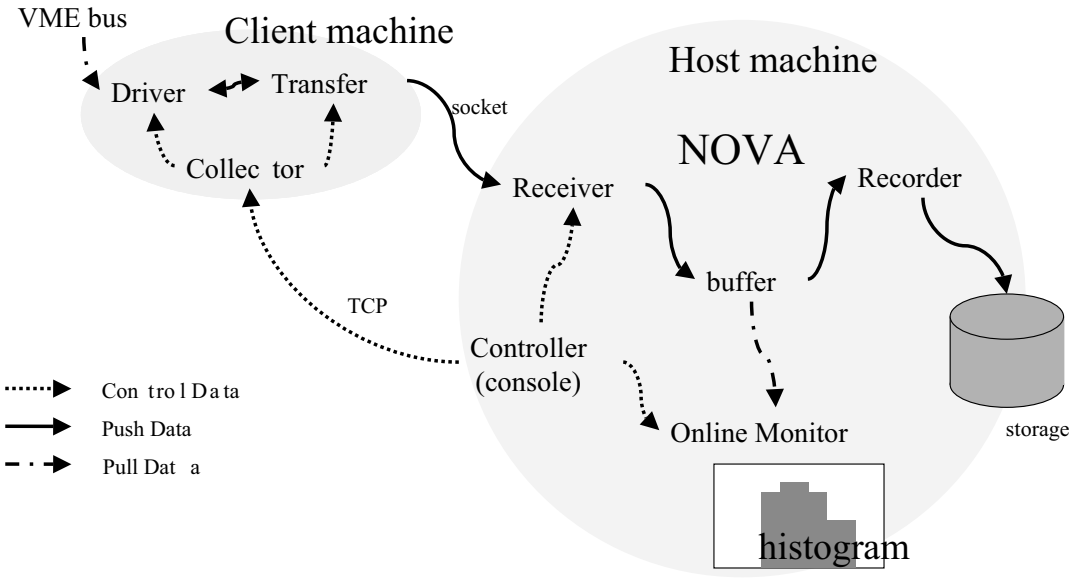

Figure A.1: Simple schematics of DAQ system. This system consists of two computers connected by 100Base-T network interface. Both computers are operated by Linux operating system.

Bibliography

[1] D. H. PERKINS, Introduction to high energy physics, Cambridge (2000)

[2] D.J. Gross, R.D. Pisarski, L.G. Yaffe, Rev. of Mod. Phys. **53** (1981) 43

[3] Krishna Rajagopal and Frank Wilczek, hep-ph/0011333 (2000)

[4] C. Vafa and E. Witten, Nucl. Phys. **B234** (1984) 173

[5] M. Dey,et al. Phys. Rev. Lett **66** (1990) 2720-2723

[6] F. Klingl and W. Weise Vector mesons in medium. (1998)

[7] T.Matsui and H.Satz Physics Letter **B178** (1986) 416

[8] P. Aurenche, R. Baier, M. Fontannaz, J. Owens, and M. Werlen, Phys. Rev. **D39** (1989) 3275

[9] G. Agakishiev et al. First results from the CERES radial TPC. Nucl. Phys. **A661** (1999) 673

[10] G. Hering Dielectron production in heavy ion collisions as 158 GeV/c per nucleon, nucl-ex/0203004

[11] G. Agakishiev et al., Nucl. Phys. **A638** (1998) 159

[12] PHENIX Conceptual Design Report, BNL, USA 1993, unpublished.

[13] PHENIX collaboration, Nucl. Phys. **A638** (1998) 565c.

[14] http://www.phenix.bnl.gov/phenix/WWW/TPCHBD/

[15] D.R.Nygren, Phys. Scripta **23** (1981) 584

[16] J.Va'vra,et al. NIM **A324** (1993) 113-126

[17] http://consult.cern.ch/writeup/magboltz/

[18] http://consult.cern.ch/writeup/heed/

[19] http://www.cern.ch/GDD/

[20] D. Mukhopadhyay,et al. Nucl. Phys. A

[21] F. Lapique and F. Piuz, Simulation of the measurement by primary cluster counting of the energy lost by a relativistic ionizing particle in argon Nucl. Inst. Meth. **175** (1980) 297

[22] Drift and Diffusion of electrons in Gases, ERRATUM TO CERN 84-08 (1984)

[23] http://consult.cern.ch/writeup/garfield/

[24] H. Okuno et al., IEEE Trans. Nucl. Sci. **NS-26** (1979) 160

[25] R. Thun, Nucl. Instr. and Meth. **A273** (1988) 157

[26] L.G. Christophorou et al., Nucl. Instr. and Meth. **163** (1979) 141

[27] http://wwwasd.web.cern.ch/wwwasd/geant/index.html

[28] http://consult.cern.ch/writeup/heed/

[29] M. Anderson et al., Nucl. Instr. and Meth. **A499** (2003) 659

[30] http://root.cern.ch/

[31] Y. Yasu, et al.: KEK-Preprint 95-84 (1995)